The Astrophysical Journal, 719:1672–1692, 2010 August 20 doi:10.1088/0004-637X/719/2/1672

BINARY QUASARS AT HIGH REDSHIFT. I. 24 NEW QUASAR PAIRS AT $z \sim 3$–4

Joseph F. Hennawi[1,2,11,12], Adam D. Myers[3,12], Yue Shen[4], Michael A. Strauss[4], S. G. Djorgovski[5], Xiaohui Fan[6], Eilat Glikman[5], Ashish Mahabal[5], Crystal L. Martin[7], Gordon T. Richards[8], Donald P. Schneider[9], and Francesco Shankar[10]

[1] Department of Astronomy, University of California at Berkeley, 601 Campbell Hall, Berkeley, CA 94720-3411, USA
[2] Max-Planck-Institut für Astronomie, Königstuhl 17, D-69117 Heidelberg, Germany
[3] Department of Astronomy, University of Illinois at Urbana-Champaign, Urbana, IL 61801, USA
[4] Princeton University Observatory, Peyton Hall, Princeton, NJ 08544, USA
[5] Astronomy Department, California Institute of Technology, Pasadena, CA 91125, USA
[6] Steward Observatory, University of Arizona, 933 North Cherry Avenue, Tucson, AZ 85721, USA
[7] Department of Physics, University of California, Santa Barbara, CA 93106, USA
[8] Department of Physics, Drexel University, 3141 Chestnut Street, Philadelphia, PA 19104, USA
[9] Department of Astronomy and Astrophysics, Pennsylvania State University, 525 Davey Laboratory, University Park, PA 16802, USA
[10] Max-Planck-Institut für Astrophysik, Karl-Schwarzschild-Str. 1, D- 85748, Garching, Germany
Received 2009 August 31; accepted 2010 January 2; published 2010 August 3

ABSTRACT

The clustering of quasars on small scales yields fundamental constraints on models of quasar evolution and the buildup of supermassive black holes. This paper describes the first systematic survey to discover high-redshift binary quasars. Using color-selection and photometric redshift techniques, we searched 8142 deg^2 of Sloan Digital Sky Survey imaging data for binary quasar candidates, and confirmed them with follow-up spectroscopy. Our sample of 27 high-redshift binaries (24 of them new discoveries) at redshifts $2.9 < z < 4.3$ with proper transverse separations 10 kpc $< R_\perp <$ 650 kpc increases the number of such objects known by an order of magnitude. Eight members of this sample are very close pairs with $R_\perp < 100$ kpc, and of these close systems four are at $z > 3.5$. The completeness and efficiency of our well-defined selection algorithm are quantified using simulated photometry and we find that our sample is ∼50% complete. Our companion paper uses this knowledge to make the first measurement of the small-scale clustering ($R < 1\ h^{-1}$ Mpc comoving) of high-redshift quasars. High-redshift binaries constitute exponentially rare coincidences of two extreme ($M \gtrsim 10^9\ M_\odot$) supermassive black holes. At $z \sim 4$, there is about one close binary per 10 Gpc^3, thus these could be the highest sigma peaks, the analogs of superclusters, in the early universe.

Key words: cosmology: observations – large-scale structure of universe – quasars: general – surveys

Online-only material: color figures

1. INTRODUCTION

Astronomers do not yet understand how quasars fit into the galaxy formation hierarchy and how they relate to the underlying structure and evolution of the dark matter. In the current paradigm, every massive galaxy is hosted by a dark matter halo and is thought to have undergone a luminous quasar phase; in this picture quasars at high redshift are the progenitors of the local dormant supermassive black holes found in the centers of all nearby bulge-dominated galaxies. This fundamental connection is supported by the tight correlations observed between the masses of central black holes and the velocity dispersions (or masses) of their old stellar populations (Magorrian et al. 1998; Ferrarese & Merritt 2000; Gebhardt et al. 2000; Tremaine et al. 2002; Häring & Rix 2004) and by the fact that the black hole mass density in the local universe is commensurate with the luminosity density produced by quasars at high redshift (e.g., Soltan 1982; Small & Blandford 1992; Yu & Tremaine 2002; Haiman et al. 2004; Marconi et al. 2004; Shankar et al. 2004, 2009a, 2009b, 2010a, 2010b; Shen 2009).

Quasars are likely to reside in massive hosts (Turner 1991) and it has been suggested that they occupy the rarest peaks in the initial Gaussian density fluctuation distribution (Efstathiou & Rees 1988; Cole & Kaiser 1989; Nusser & Silk 1993; Djorgovski 1999; Djorgovski et al. 1999). It is also thought that quasar activity is triggered by the frequent galaxy mergers which are a generic consequence of bottom up structure formation (Carlberg 1990; Haehnelt & Rees 1993; Barnes & Hernquist 1996; Bahcall et al. 1997; Thacker et al. 2006; Hopkins et al. 2008; Wetzel et al. 2009a, 2009b), and merger-based models provide a good description of many of the observed aggregate properties of the quasar population (Haiman & Loeb 1998; Cavaliere & Vittorini 2000; Kauffmann & Haehnelt 2000; Wyithe & Loeb 2002; Thacker et al. 2006; Hopkins et al. 2006; Thacker et al. 2008; Shen 2009).

In a hierarchical universe, the large-scale clustering of a population of objects is directly related to their host dark matter halo masses (Cole & Kaiser 1989; Mo & White 1996). Hence, measuring quasar clustering probes the relationship between quasar luminosity and halo mass, providing constraints on the quasar lifetime or duty cycle (Cole & Kaiser 1989; Haiman & Hui 2001; Martini & Weinberg 2001, but see Wyithe & Loeb 2008), physical parameters governing black hole fueling such as the radiative efficiency and Eddington ratio (Wyithe & Loeb 2005; Shankar et al. 2008, 2010a; Shen 2009), and the scatter in these parameters (White et al. 2008). The advent of

[11] NSF Astronomy and Astrophysics Postdoctoral Fellow.
[12] Visiting Astronomer, Kitt Peak National Observatory, National Optical Astronomy Observatory, which is operated by the Association of Universities for Research in Astronomy (AURA) under cooperative agreement with the National Science Foundation.

large spectroscopic quasar surveys has led to firm constraints on the clustering (Porciani et al. 2004; Croom et al. 2005; Myers et al. 2006, 2007a; da Ângela et al. 2008; Padmanabhan et al. 2009; Shen et al. 2007, 2009; Ross et al. 2009) of quasars at $z \lesssim 2.5$—like luminous galaxies, quasars show little apparent clustering evolution with redshift. In addition, the first estimates of the dependence of clustering on luminosity (Porciani & Norberg 2006; Shen et al. 2009), redshift (Shen et al. 2007), the presence of broad-absorption line (BAL) troughs (Shen et al. 2008a), and radio brightness (Shen et al. 2009) have been made. The cross-correlation of quasars with galaxies has also resulted in complementary constraints (Adelberger & Steidel 2005a, 2005b; Serber et al. 2006; Coil et al. 2007; Padmanabhan et al. 2009).

The clustering of high-redshift quasars is much more challenging to measure (Kundic 1997; Stephens et al. 1997) because they are intrinsically rare. But the Sloan Digital Sky Survey (SDSS; York et al. 2000) has recently enabled a measurement of quasar clustering on large scales at $z > 3$. Shen et al. (2007) measured the clustering of quasars from $2.9 \leqslant z \leqslant 5.4$ using a sample of $\gtrsim$4000 quasars selected from the SDSS DR5 (Adelman-McCarthy et al. 2007). Dividing their sample into two redshift bins, they measured comoving correlation lengths ($\gamma = 2$) of $r_0 = 16.9 \pm 1.7\ h^{-1}$ Mpc and $r_0 = 24.3 \pm 2.4\ h^{-1}$ Mpc, for $2.9 \leqslant z \leqslant 3.5$ and $z > 3.5$, respectively. Thus, $z > 3$ quasars cluster much more strongly than their $z \lesssim 2.5$ counterparts ($r_0 \simeq 7\ h^{-1}$ Mpc), implying that high-redshift quasars are highly biased and inhabit very massive ($M \gtrsim 10^{13}\ h^{-1}\ M_\odot$) dark matter halos. These large-scale clustering constraints at low and high redshift now play a fundamental role in our understanding of the quasar evolution and the buildup of supermassive black holes (Thacker et al. 2006, 2008; Lidz et al. 2006; Hopkins et al. 2007a, 2008; Djorgovski et al. 2008; White et al. 2008; Shankar et al. 2010a; Shen 2009).

Quasar clustering on small scales ($R < 200$ kpc proper) yields independent and complementary constraints on quasar evolution. Djorgovski (1991) first suggested that the handful of binary quasars known at the time implied a factor of ~100 larger clustering amplitude on scales $R < 50$ kpc than predicted by naively extrapolating the quasar correlation function power law from larger scales, and proposed that this was due to the enhancement of quasar activity during merger events. Hennawi et al. (2006b) conducted an extensive follow-up campaign to find companions of SDSS quasars, providing the first measurement of the quasar correlation function on scales $10\ h^{-1}$ kpc $< R_{\rm prop} < 400\ h^{-1}$ kpc. For $R_{\rm prop} \lesssim 50\ h$ kpc, they detected an order of magnitude higher clustering than the expectation from the larger-scale quasar correlation function extrapolated as a power law, providing compelling evidence that the quasar correlation function steepens on sub-Mpc scales. This result has since been confirmed with better accuracy using more homogeneous selected photometric (Myers et al. 2007b) and spectroscopic samples (Myers et al. 2008), albeit with less excess over a power law. Additional circumstantial evidence for enhanced small-scale clustering comes from the recent discovery of the first triple quasar (Djorgovski et al. 2007). Similarly large small-scale clustering may be present around low-redshift active galactic nuclei (AGNs) at $z < 0.6$ (Serber et al. 2006; Strand et al. 2008, but see Padmanabhan et al. 2009). Motivated by these small-scale measurements, several theoretical investigations have argued that excess small-scale clustering occurs naturally if quasar activity is triggered by mergers (Thacker et al. 2006, 2008; Hopkins et al. 2008; Wetzel et al. 2009b) and have considered the constraints that small-scale clustering measurements place on how quasars populate their dark matter halos (Wetzel et al. 2009b; Shankar 2009).

Measuring small-scale quasar clustering is of particular interest at high redshifts ($z > 3$), where the population of supermassive black holes powering quasars is rapidly growing and the large-scale clustering indicates that quasars are hosted by extremely massive dark matter halos ($M \gtrsim 10^{13}\ h^{-1}\ M_\odot$), which are the progenitors of today's rich clusters. Could the mechanism that triggers the growth of these extreme black holes ($M \gtrsim 10^9\ M_\odot$ at high redshift) be different from that at lower redshifts? Are $z \sim 4$ quasars always at the center of their host dark matter halo, or can they be hosted by less massive satellites? If a high-redshift binary quasar represents an exponentially rare coincidence of two extremely massive black holes (and dark matter halos/subhalos), are these the highest sigma peaks, the analogs of superclusters, in the early universe? The evolution of small-scale clustering to high redshift can shed light on all of these questions. However, even in the large $z > 3$ quasar sample studied by Shen et al. (2007), the smallest scale at which the correlation function can be measured is $\sim 2\ h^{-1}$ Mpc. The reason for this is twofold. First, close quasar pairs with angular separations $\lesssim 60''$ ($\sim 1.5\ h^{-1}$ Mpc at $z \sim 4$), are extremely rare—the mean quasar separation at $z > 3$ is $\sim 150\ h^{-1}$ Mpc and at small separations, the correlation function does not increase as fast as the volume decreases. Second, because of the finite size of the optical fibers of the SDSS multi-object spectrograph, only one quasar in a close pair with separation $<55''$ can be observed on a given plate[13] (Blanton et al. 2003). The only subarcminute high-redshift quasar pair in the literature is a $33''$ pair of quasars at $z = 4.25$ discovered serendipitously by Schneider et al. (2000). Djorgovski et al. (2003) discovered a quasar at $z = 5.02$ $196''$ away from the high-redshift quasar at $z = 4.96$ discovered by Fan et al. (1999), corresponding to a proper transverse separation of 900 h^{-1} kpc. This is the highest redshift pair of quasars known.

In this paper, we present the results of a systematic survey to discover high-redshift binary quasars and measure the small-scale clustering of quasars at $z \sim 3$–4 for the first time. Using color-selection and photometric redshift techniques, we searched the SDSS photometric data for binary quasar candidates, which we confirmed spectroscopically with follow-up observations. The outline of this paper is as follows. In Section 2, we present our algorithm for finding high-redshift binary quasars candidates in the SDSS photometric data, and quantify the completeness and efficiency of our search. Our spectroscopic follow-up observations are described in Section 3, and the binary quasar sample is presented in Section 4, where we also summarize the status of our survey. We summarize and conclude in Section 5. In a companion paper (Shen et al. 2010, henceforth Paper II), we use the binaries presented here to measure the small-scale ($R < 1\ h^{-1}$ Mpc comoving) clustering of high-redshift quasars.

Throughout this paper, we use the best-fit *Wilkinson Microwave Anisotropy Probe* (*WMAP*) cosmological model of Dunkley et al. (2009), with $\Omega_m = 0.26$, $\Omega_\Lambda = 0.74$, and $h = 0.7$. Because both proper and comoving distances are used in this paper, we will always explicitly indicate proper distances (quoted in kpc). It is helpful to remember that in the chosen cosmology, for a typical quasar redshift of $z = 3.5$, an angular

[13] An exception to this rule exists for a fraction (~30%) of the area of the SDSS spectroscopic survey covered by overlapping plates. Because the same area of sky was observed spectroscopically on more than one occasion, there is no fiber collision limitation for these regions.

separation of $\Delta\theta = 1''$ corresponds to a proper transverse separation of $R_\perp = 7.6$ kpc (comoving $R_\perp = 24.1\ h^{-1}$ kpc), and a velocity difference of 1000 km s^{-1} at this redshift corresponds to a proper radial redshift space distance of $s_\parallel = 2.9$ Mpc (comoving $s_\parallel = 9.1\ h^{-1}$ Mpc). All magnitudes quoted are SDSS asinh magnitudes (Lupton et al. 1999). To avoid confusion between redshift and z-band magnitude, we will always use a text "z" to denote redshift.

2. FINDING BINARY QUASARS

Because binary quasars at $z \gtrsim 3$ are extremely rare, we must target candidates to $i = 21$, as faint as the SDSS imaging data will allow, to build up statistics. This flux limit is significantly fainter than the SDSS spectroscopic flux limit ($i < 20.2$), and because fiber collisions exclude close pairs in SDSS spectroscopy, we must select binary candidates from the imaging data and then follow them up spectroscopically. Finding binary quasars thus amounts to constructing a *photometric* quasar catalog with a high completeness and efficiency at faint magnitudes.

Our algorithm for selecting $z > 3$ binary quasars evolved somewhat over the course of our survey. We experimented with different approaches, such as searching for companions only around spectroscopically confirmed quasars following Hennawi et al. (2006b), searching for pairs in the photometric quasar catalog of Richards et al. (2009, see also Richards et al. 2004), and constructing our own photometric quasar catalog. The final algorithm adopted is an amalgam of these methods and we describe it in detail in what follows. In Section 2.1, we provide details of the SDSS spectroscopic quasar sample. Many of our binary candidates have one member bright enough for the spectroscopic survey, and these data are used whenever possible. The photometric quasar catalog of Richards et al. (2009) is described in Section 2.2. This catalog did not perform well enough at high redshift to be our sole selection algorithm, however, we utilize it in an auxiliary manner to improve the efficiency of our search. An important step in understanding the completeness of our binary selection was the construction of simulated quasar data, as we describe in Section 2.3. The core of our selection algorithm is the construction of a photometric quasar catalog which carefully treats photometric errors, which we introduce in Section 2.4 and apply to the SDSS imaging data in Section 2.5. The final algorithm for selecting binaries is presented in Section 2.6, where we also estimate the completeness of our search—a necessary step for the small-scale quasar clustering constraints presented in Paper II.

2.1. The SDSS Spectroscopic Quasar Sample

The SDSS uses a dedicated 2.5 m telescope (Gunn et al. 2006) and a large format CCD camera (Gunn et al. 1998) at the Apache Point Observatory (APO) in New Mexico to obtain images in five broad bands (u, g, r, i, and z, centered at 3551, 4686, 6166, 7480, and 8932 Å, respectively; Fukugita et al. 1996; Stoughton et al. 2002) of high Galactic latitude sky in the Northern Galactic Cap. The imaging data are processed by the astrometric pipeline (Pier et al. 2003) and photometric pipeline (Lupton et al. 2001), and are photometrically calibrated to a standard star network (Smith et al. 2002; Tucker et al. 2006; Padmanabhan et al. 2008). Additional details on the SDSS data products can be found in the data release papers (e.g., Abazajian et al. 2003, 2004, 2005).

Quasar candidates are targeted for follow-up spectroscopy based on colors measured from the SDSS imaging data (Richards et al. 2002b). These candidates along with other targets (i.e., galaxies, stars, serendipity), are observed with two double spectrographs producing spectra covering 3800–9200 Å with a spectral resolution ranging from 1800 to 2100. Details of the spectroscopic observations can be found in York et al. (2000), Castander et al. (2001), and Stoughton et al. (2002). Quasars observed through the Fifth Data Release (Adelman-McCarthy et al. 2007) have been cataloged by Schneider et al. (2007, see also Schneider et al. 2005).

High-redshift quasars are optically unresolved and thus cannot be distinguished from stars based on image morphology. The majority of quasar candidates are selected based on their location in the multidimensional SDSS color space. All magnitudes are reddening corrected following the prescription in Schlegel et al. (1998). Objects with colors that place them far from the stellar locus and which do not inhabit specific "exclusion" regions (e.g., places dominated by white dwarfs, A stars, and M star-white dwarf pairs; Smolčić et al. 2004) are identified as primary quasar candidates. An i magnitude limit of 19.1 is imposed for candidates whose colors indicate a probable redshift of less than ≈ 3, while higher redshift candidates are targeted if $i < 20.2$. The colors of quasars become difficult to distinguish from F stars at $z \approx 2.7$ (Fan 1999; Richards et al. 2001a), which significantly lowers the efficiency of quasar target selection. The SDSS quasar target selection therefore deliberately sparse samples in that region of color space, resulting in high incompleteness (Richards et al. 2002b, 2006) near this redshift. We therefore focus our high-redshift binary quasar search at $z \geqslant 2.9$.

2.2. The SDSS KDE Photometric Sample

Richards et al. (2004) and Richards et al. (2009) have constructed faint ($i \lesssim 21$) photometric samples of quasars from the SDSS photometry alone, by separating quasars from stars using knowledge of their relative densities in color space. A technique known as Kernel Density Estimation (henceforth KDE, or "the KDE technique") uses training sets of quasars and stars to obtain non-parametric estimates of their respective densities in color space. Then a probability can be assigned for any photometric object of interest for being quasar like, or star like. Objects with quasar-like probability above a threshold are selected as photometric quasars, and are assigned a photometric redshift, and a probability that the photometric redshift is correct (Weinstein et al. 2004). The most recent Richards et al. (2009) photometric quasar catalog of (henceforth the DR6 KDE catalog) covers the 8417 deg^2 area corresponding to the SDSS Data Release 6 (DR6; Adelman-McCarthy et al. 2008), extends down to an extinction-corrected flux limit of $i < 21.3$, and attempts to classify quasars over the full range of redshifts accessible to the SDSS imaging, $0 < z \lesssim 5.5$.

The fundamental drawback of the KDE approach is that the probabilities of an object being quasar like or star like do not take into account photometric errors. At faint magnitudes where errors become large, the KDE catalog suffers from incompleteness which is not currently understood. Since a quantitative estimate of the completeness of our selection is necessary to place constraints on small-scale quasar clustering, using the KDE catalog alone as our selection algorithm is insufficient. Of the 27 $z > 2.9$ binary quasars in the SDSS footprint (see Table 3), 25 have both members bright enough to be in the KDE catalog. Of these, 17 have both members in the

KDE catalog and the other eight have only one member in the KDE.

2.3. Simulated Binary Quasars

Our binary survey extends to $i = 21$, and because of photometric errors, the completeness decreases to fainter magnitudes. Hence, we need to generated simulated binary quasars to determine our completeness, as we do not have a large sample of spectroscopically confirmed $z > 2.9$ quasars at magnitudes fainter than the SDSS quasar survey flux limit of $i = 20.2$.

It will prove to be convenient if the simulated quasars have an approximately correct redshift and number count distribution. Even at bright magnitudes, the redshift and magnitude distribution of the SDSS quasar sample has the selection function of the targeting algorithm imprinted on it. In particular, the SDSS spectroscopic sample suffers high incompleteness at $z = 2.7$–3.0 and at $z \simeq 3.4$ (see Figure 8 of Richards et al. 2006). Instead, we determine the redshift and number count distribution from the measured quasar luminosity function (LF). Usable LFs for quasars at redshift $2.9 < z < 4.5$ which probe the faint apparent magnitudes ($i < 21$) include Wolf et al. (2003), Jiang et al. (2006), Richards et al. (2006), and Hopkins et al. (2007b). After comparing all of these results, we decided on a combination of the Jiang et al. (2006) LF fits (at $z < 3.5$) and the COMBO-17 PDE (Wolf et al. 2003) fits (at $z > 3.5$) for the model LF, and scaled the result to our standard cosmology. We refer the reader to Paper II for additional details of the adopted LF.

Our procedure for simulating binary quasars is then as follows.

1. Draw a quasar redshift z from the redshift distribution $dN/dz(i < 21)$ determined by integrating the LF.
2. Given this redshift, draw two magnitudes, i_1 and i_2, for the two members of the binary from the apparent magnitude distribution of quasars at this redshift, $n(z, < i)$.
3. If $i_1 \leqslant 20.2$, locate a quasar in the real SDSS quasar sample with a similar value of i and z. Use the real quasar photometry for the first quasar.
4. If $i_1 > 20.2$, then locate a quasar in the real SDSS quasar sample with well-measured colors ($i < 19.5$) and similar z. Make the real quasar fainter by scaling all five fluxes f^m, $m = (u, g, r, i, z)$, by the implied ratio of i-band fluxes. Add Gaussian noise to the scaled fake data with standard deviation $\sigma^m(f^m)$ consistent with the SDSS noise model (see below).
5. Use same procedure to generate photometry for the second member of the binary.

Note that because the aforementioned procedure is based on real quasar photometry at a given redshift, the effect of Lyα forest and Lyman-limit system absorption on quasar colors are automatically modeled correctly.

To model the noise in the photometry as a function of flux level in filter m, $\sigma^m(f^m)$, we randomly select 10^6 stellar objects from the SDSS photometric data and apply a running median filter. Given a five-dimensional (*ugriz*) flux vector f^m for a simulated quasar, we then add random Gaussian noise. Note that our procedure assumes no covariance between the flux noise in different filters, which is a good approximation for point sources (Scranton et al. 2005). As an example, a randomly chosen simulated quasar at $z = 3.2$ with $i = 20.2$ has $m = (23.00, 20.66, 20.32, 20.20, 20.00)$ and $\sigma = (0.47, 0.025, 0.026, 0.034, 0.082)$, where these values represent real photometric data (since $i \leqslant 20.2$). Similarly, at $z = 4$ we simulate an object with $m = (24.68, 21.58, 20.28, 20.20, 20.21)$ and $(0.87, 0.058, 0.027, 0.033, 0.12)$. For quasars at the same redshifts but with $i = 21$, again chosen at random, we have example objects with $m = (23.27, 21.42, 20.91, 21.00, 20.83)$ and $\sigma = (0.66, 0.053, 0.047, 0.072, 0.21)$ at $z = 3.2$, and $(25.92, 22.83, 21.12, 21.00, 21.10)$ and $\sigma = (0.70, 0.17, 0.055, 0.072, 0.26)$ at $z = 4$.

2.4. Locus Distances

2.4.1. The Quasar Locus

Although quasars have a wide range of luminosities, the majority of unobscured quasars have similar optical/ultraviolet spectral energy distributions. Richards et al. (2001a) demonstrated that most quasars follow a tight color–redshift relation in the SDSS filter system, a property which has been exploited to calculate photometric redshifts of quasars (Richards et al. 2001b; Budavári et al. 2001; Weinstein et al. 2004). It is thus possible to efficiently target binary quasars by searching for pairs of objects with similar, quasar-like colors (Hennawi 2004; Hennawi et al. 2006b). But stars are a significant contaminant and must be avoided: for $i < 19$ stars outnumber quasars on the sky by a factor of $\gtrsim$50 (e.g., Yasuda et al. 2001; Sesar et al. 2007) even at high galactic latitudes, although stars are less dominant at fainter magnitudes (factor $\sim$25 for $i < 21$). The vast majority of stars detected by SDSS are on the main sequence (>98%; Finlator et al. 2000; Helmi et al. 2003; Jurić et al. 2008) and form an extremely tight well-defined temperature sequence (Ivezić et al. 2004), referred to as the stellar locus in color–color diagrams. Hence, quasars can be selected efficiently by targeting unresolved objects near the quasar locus but far from the stellar locus, except at redshift $z \approx 2.7$ and $z = 3.4$ where the two loci cross (Fan 1999; Richards et al. 2001a, 2006).

As objects become progressively fainter, photometric measurement errors blur the distinction between the quasar and stellar loci. The SDSS quasar spectroscopic target selection algorithm (Richards et al. 2002b) is not well-suited for such faint objects ($i \sim 21$), and as discussed in Section 2.2 the DR6 KDE catalog is not well characterized at these faint magnitudes either. Hence, we introduce a new algorithm for selecting high-redshift quasars focusing on a proper statistical treatment of photometric errors. Following Hennawi et al. (2006b), we define a statistic that quantifies the likelihood that an astronomical object has colors consistent with a given model, based on the mean quasar color–redshift relation and the stellar locus.

Given the fluxes of an object in the five SDSS bands $f^m_{\rm data}$, we ask whether they are consistent with proportionality to a model

$$f^m_{\rm data} = A f^m_{\rm model}, \tag{1}$$

where $f^m_{\rm model}$ is a five-dimensional vector of model fluxes, and this relationship holds for a single proportionality constant in all bands. For the quasar locus, the model will be the average run of scaled quasar flux with redshift $f^m_{\rm model}(z)$, whereas for the stellar locus the model will be the scaled stellar flux as a function of surface temperature.

For a quasar, the maximum likelihood value of the parameters A and z, given measured fluxes $f^m_{\rm data}$, can be determined by χ^2 minimization:

$$\chi^2(A, z) = \sum_{\rm ugriz} \frac{\left[f^m_{\rm data} - A f^m_{\rm model}(z)\right]^2}{\left[\sigma^m_{\rm data}\right]^2 + A^2\left[\sigma^m_{\rm model}(z)\right]^2}, \tag{2}$$

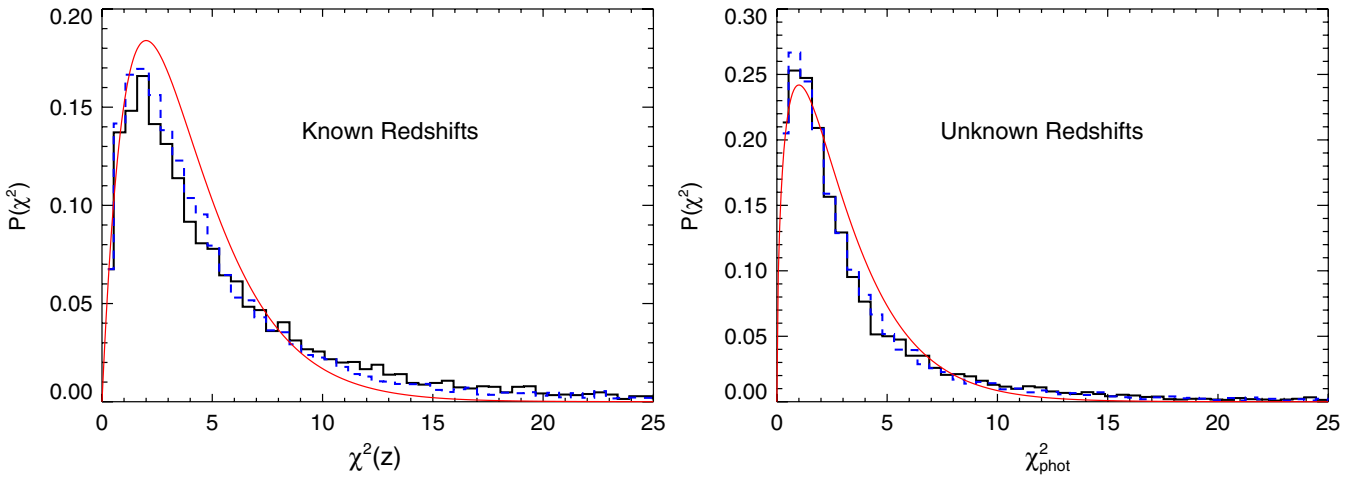

Figure 1. Histograms of quasar locus distance statistics. The left panel shows the distribution of $\chi^2(z)$, where redshift was taken to be known and Equation (2) was minimized for A only. The right panel shows the distribution of $\chi^2_{\rm phot}$, i.e., minimized with respect to both amplitude A and redshift z. The solid (black) histograms are distributions for the 6696 $i < 20.2$ training sample quasars at $z > 2.5$ used to fit the flux–redshift relation. The dashed (blue) histograms are from ∼600,000 fainter ($i < 21$) simulated quasars at $z > 2.5$. The solid (red) curve shows the χ^2_4 distribution in the left panel and the χ^2_3 in the left panel.

(A color version of this figure is available in the online journal.)

where $\sigma^m_{\rm data}$ are the photometric measurement errors and $\sigma^m_{\rm model}(z)$ is the intrinsic 1σ scatter about the mean quasar flux–redshift relation, both presumed to be Gaussian distributed. The assumption of Gaussian statistics is valid for the measurement errors (Scranton et al. 2005), but Richards et al. (2001a) found a red tail in the distribution of quasar colors about the mean, which is due to dust extinction (Richards et al. 2003; Hopkins et al. 2004).

To compute $f^m_{\rm model}(z)$ we follow Richards et al. (2001a) to fit the mean color–redshift relation for quasars, but instead of fitting colors we rescale all the f^m to have the same value of $f^r + f^i + f^z$ (and σ^m rescaled accordingly), and fit $f^m_{\rm model}(z)$. This procedure is preferable to fitting colors for two reasons. First, for high-redshift quasars that have dropped out of a filter, say u band, forming the $u-g$ color degrades a high signal-to-noise ratio (S/N) g-band measurement with the noisy u-band measurement. Second, at low S/Ns Pogson magnitudes or SDSS asinh magnitudes (Lupton et al. 1999) pose several disadvantages, such as bias in the resulting colors and non-Gaussian error distributions, whereas the rescaled fluxes are immune from these problems.

To fit $f^m_{\rm model}(z)$, we start with a sample of ∼77, 000 quasars in the SDSS DR5 quasar catalog (Schneider et al. 2007). Restricting attention to quasars in the redshift range $0.3 \leqslant z \leqslant 5.5$, removing BAL quasars (which would bias the mean colors), and restricting attention to quasars with well-measured redshifts (see Shen et al. 2008b) and the most accurate photometry, results in a sample of 52,000 quasars, including 5143 quasars with $z > 2.9$ and 829 with $z > 4$. Fluxes are galactic extinction-corrected following the prescription in Schlegel et al. (1998) and rescaled to have the same value of $f^r + f^i + f^z$. The rescaled flux in each band is then fitted as a function of redshift z using a fourth-order B-spline with a breakpoint spacing of 0.1 and outlier rejection. Given this mean flux–redshift relation $f^m_{\rm model}(z)$, we then determine the 1σ scatter about it, $\sigma^m_{\rm model}(z)$, by applying a running median filter to the difference between the data and the fits, $f^m - f^m_{\rm model}(z)$, sorted by redshift. By construction this median curve brackets 50% of the data points and varies smoothly with redshift. The 1σ scatter is then determined from the median curve by rescaling the median by the appropriate factor to enclose 68% of the data points for a Gaussian distribution. Our estimate of $\sigma^m_{\rm model}(z)$ is clearly approximate since it assumes Gaussian statistics, and includes a significant contribution from photometric errors from the fainter objects.

If the redshift of the quasar is known, minimizing χ^2 with respect to A results in four degrees of freedom (the number of independent colors that can be formed from five fluxes) and χ^2 should follow the χ^2_4 distribution. If instead z is unknown, it can be estimated by minimizing χ^2. However, the resulting distribution of χ^2 values will be close to χ^2_3, but not exactly because the colors are not a linear function of z.[14]

The histograms in the left panel of Figure 1 show the resulting distribution of $\chi^2(z)$ when the $f^m_{\rm model}(z)$ is evaluated at the true redshift of the quasar. The solid (black) histogram is the distribution of χ^2 for the subset of the training sample used to fit the quasar flux–redshift relation, which have $i < 20.2$ and $z > 2.5$ (6696 quasars). The dashed (blue) histogram is the distribution of χ^2 for a sample of ∼600,000 fainter simulated quasars with $i < 21$ (see Section 2.3). The solid (red) curve shows the χ^2_4 distribution. The median value of χ^2 for the real data is 3.93 and it is 3.63 for the simulated data, whereas the median of the χ^2_4 distribution is 3.37. Our training set (solid histogram) is broader than the χ^2_4 distribution (solid curve) and exhibits a tail toward large values, presumably because of the non-Gaussian tail of the quasar color distribution (Richards et al. 2001a). For the fainter simulated sample, the scatter about the mean becomes more dominated by photometric measurement errors rather than intrinsic color variations, and the distribution is closer to χ^2_4.

The distribution of χ^2 minimized with respect to both parameters, A and z, is shown in the right panel of Figure 1. This number quantifies the likelihood that a quasar has photometric redshift z, and we denote it as $\chi^2_{\rm phot}$. As expected, the resulting distributions of $\chi^2_{\rm phot}$ are significantly narrower than before, with median values of 2.19 and 2.17 for the training sample and fainter simulations, respectively, which can be compared to the median of the χ^2_3 distribution, 2.38. The performance of our photometric redshift algorithm for high-redshift quasars

[14] Recall that minimizing χ^2 with respect to a parameter reduces the number of degrees of freedom by one only if χ^2 is linear in that parameter.

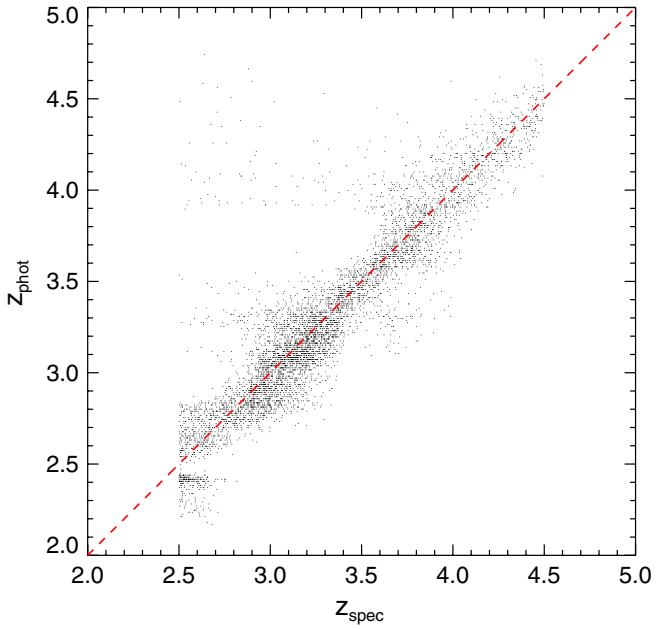

Figure 2. Photometric redshift vs. spectroscopic redshift for quasars with $2.5 < z < 4.5$ in our training sample ($i \lesssim 20.2$). For $z > 2.9$, 83% of the training set quasars and 81% of the fainter ($i < 21$) simulated quasars have $|z - z_{\rm phot}| < 0.2$. The standard deviation (with outlier rejection) is $\sigma_z = 0.14$ for the training set and $\sigma_z = 0.15$ for the fainter simulated data.

(A color version of this figure is available in the online journal.)

is illustrated in Figure 2, where we plot photometric redshift versus spectroscopic redshift for quasars in the training sample with $2.5 < z < 4.5$. Our photometric redshifts are very accurate for high-redshift quasars, except and $z < 2.7$ where we tend to underestimate the true redshift. This degeneracy with lower photometric redshifts is likely due to poor S/N in the u band. The primary lever arm for $z > 2$ photometric redshifts comes from filters bracketing the Lyα forest spectral break, which falls in u for $z < 2.7$. For the quasars with $2.9 < z < 4.5$ of interest for the binary selection in this paper, we find that 83% of the real training set quasars and 81% of the fainter simulated quasars have $|z - z_{\rm phot}| < 0.2$. Computing the standard deviation with outlier rejection, we find that $\sigma_z = 0.14$ for the training set data and $\sigma_z = 0.15$ for the fainter simulated data.

2.4.2. The Stellar Locus

We use a procedure similar to that used for the quasar locus to define the stellar locus. First we isolate a set of representative stars with accurate photometry using a set of SDSS spectroscopic plates on which all point sources were targeted above a flux limit of $i < 19.1$ regardless of color (see Adelman-McCarthy et al. 2006). After applying cuts to remove objects with noisy photometry and stars at the extremes of the color distribution, we arrive at a set of 13,837 spectroscopically confirmed stars with precise SDSS photometry. We parameterize the path these stars follow through the five-dimensional SDSS filter space using the $g-i$ color, a decent proxy for stellar temperature. Our fit for $f^m_{\rm model}(g-i)$ uses the same methodology as we did for the quasar locus: we rescale all stars to have the same value of $f^r + f^i + f^z$, and each band f^m is fitted with a B-spline as a function of $g-i$. The error $\sigma^m_{\rm model}(g-i)$ is more subtle than for the stellar locus. The intrinsic width of the stellar locus is so small ($\sim$0.02 mag; Ivezić et al. 2004) that the scatter in our star data about the mean relation is completely dominated by photometric measurement errors, even at $i < 19.1$. Hence, we simply use $\sigma^m_{\rm model}(g-i)$ as a floor on the error to prevent extreme values of χ^2 for rare cases of extremely high S/N photometry.

The histogram in the left panel of Figure 3 shows the distribution of χ^2 from the sample of stars which was used to fit the stellar locus, where $f^m_{\rm model}(g-i)$ was evaluated at the observed value of the $g-i$ for each star. The (red) curve shows the χ^2_4 distribution. The distribution of the data differs significantly from χ^2_4: the median value of the χ^2 for the training set is 4.35 compared to a median of 3.37 for the χ^2_4 distribution. This difference is due to a tail of stars with atypical colors, probably arising from unusual metallicities or surface gravities. In addition, intrinsic stellar colors depend on apparent magnitude, as the properties of stars change with distance, whereas our fits ignore any such dependence.

The *minimum distance* to the stellar locus, which we designate $\chi^2_{\rm star}$, can be computed by minimizing $\chi^2(A, g-i)$ with respect to both parameters. The statistical significance of an outlier from the stellar locus is quantified by $\chi^2_{\rm star}$. The right panel of Figure 3 shows the distribution of $\chi^2_{\rm star}$ compared to the χ^2_3 distribution. Requiring $\chi^2_{\rm star}$ be larger than a specified value is an effective means of reducing stellar contamination from quasar selection.

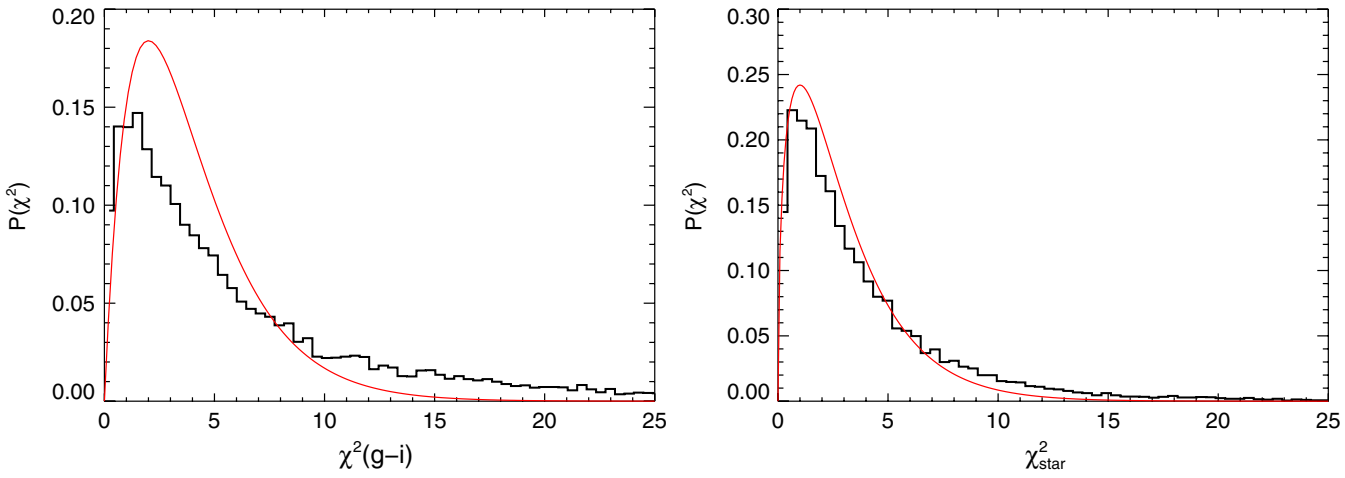

Figure 3. Histograms of stellar locus distance statistics for 13,837 spectroscopically confirmed stars with $i < 19.1$. The left panel shows the distribution of $\chi^2(g-i)$ if Equation (2) is minimized for amplitude A only. The right panel shows the distribution of the *minimum distance* to the stellar locus, whereby $\chi^2(A, g-i)$ is minimized with respect to both parameters. The (red) curves shows the χ^2_4 and χ^2_3 distributions in the left and right panels, respectively.

(A color version of this figure is available in the online journal.)

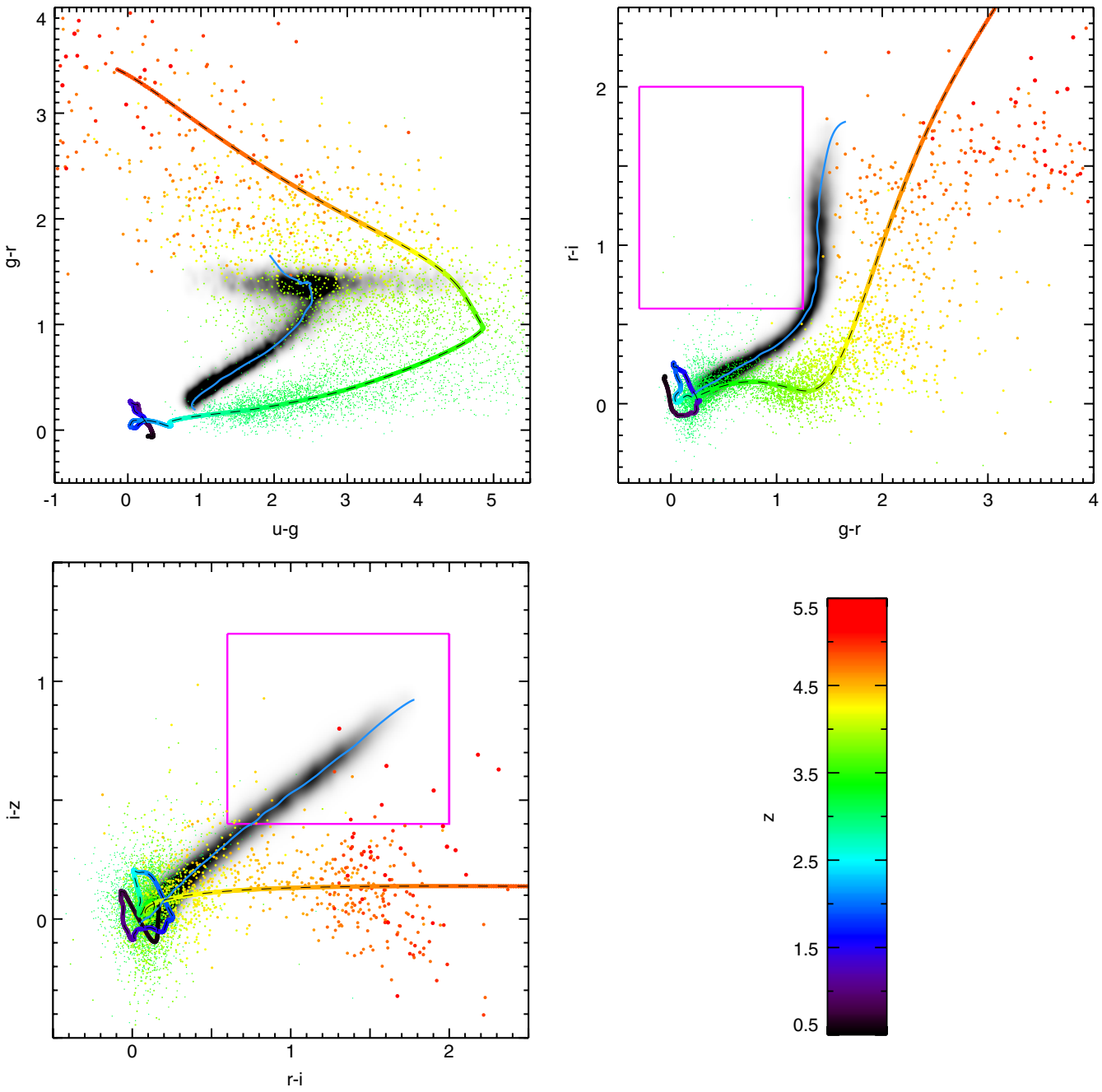

Figure 4. Color–color diagrams illustrating the stellar locus and the quasar locus. The gray shaded region denotes stellar density for the ∼14,000 stars used to fit the stellar locus, with darker regions corresponding to higher density. The light blue curve is our fit to the stellar locus. The ∼5000 $z \geqslant 2.9$ ($i \lesssim 20.2$) quasars in our training set are plotted as redshift color-coded points according to the color bar at the lower right (lower redshift quasars are omitted for clarity). Higher redshift objects are plotted as larger points. The quasar locus is shown by the dashed black line, similarly color coded to indicate redshift. The magenta square box corresponds to a region excluded from SDSS quasar selection, which we similarly exclude (see Section 2.5), because of contamination from white dwarf + M-star pairs (see Richards et al. 2001a).

(A color version of this figure is available in the online journal.)

To visualize how quasars and stars objects move through the four-dimensional SDSS color space ($u-g$, $g-r$, $r-i$, $i-z$), we plot our fits to the quasar and stellar loci in the three color–color diagrams in Figure 4.

2.5. Faint Photometric Quasar Selection

We construct a photometric quasar catalog targeting objects consistent with the quasar locus, that is small $\chi^2_{\rm phot}$, and inconsistent with the stellar locus, hence large $\chi^2_{\rm star}$. Of our simulated $i < 21$ quasars with $2.9 < z < 4.5$, 94% have $\chi^2_{\rm phot} < 10$ (see Figure 1), hence we can achieve a sample with high completeness by imposing this cut on quasar locus distance. To determine the placement of the cut on stellar locus distance consider the left panel of Figure 5. The histograms show the completeness as a function of redshift for varying limits on $\chi^2_{\rm star}$ as determined from our ∼600,000 simulated quasars with $i < 21$ and $z \geqslant 2.9$. Specifically, from top to bottom the five histograms represent $\chi^2_{\rm star} \geqslant [0, 5, 10, 15, 40]$. In addition to the cut on $\chi^2_{\rm star}$ we have imposed $\chi^2_{\rm phot} < 10$ and several other

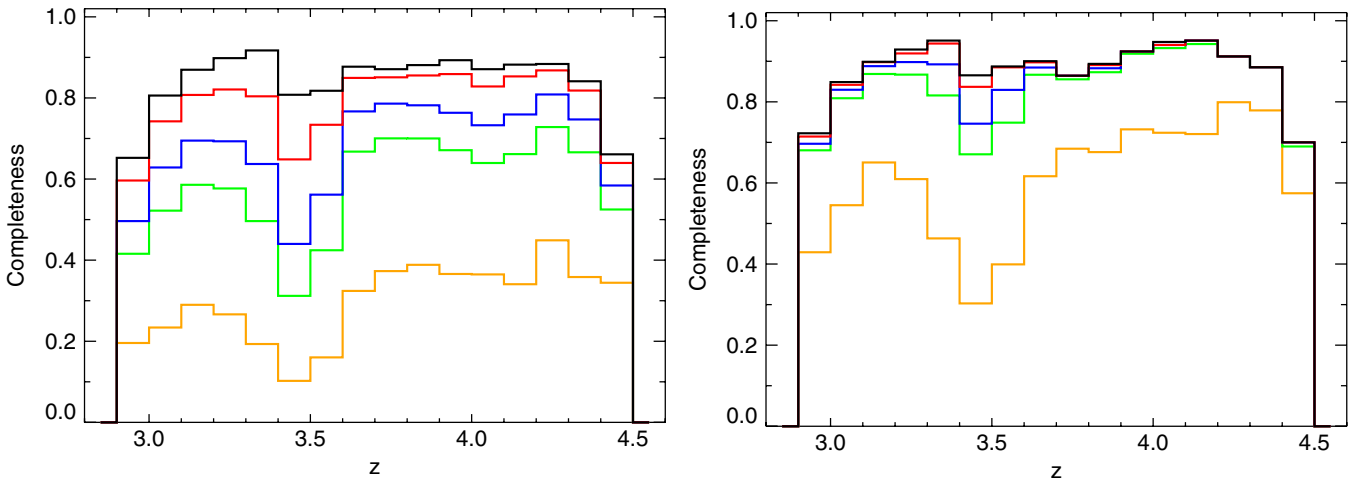

Figure 5. Completeness of the faint photometric quasar catalog as a function of redshift for varying limits on $\chi^2_{\rm star}$. All criteria in Section 2.5 have been applied except criterion 11 on $\chi^2_{\rm star}$, which varies from top to bottom as $\chi^2_{\rm star} \geqslant [0, 5, 10, 15, 40]$. The left panel shows completeness determined from ∼600,000 simulated quasars with $i < 21$. The right panel shows the completeness if we restrict to quasars with $i < 20.2$.

(A color version of this figure is available in the online journal.)

auxiliary cuts (described in detail below) which have less of an impact on the overall completeness than $\chi^2_{\rm phot}$.

If there is no constraint on $\chi^2_{\rm star}$ (upper black curves in Figure 5) the other cuts result in a total completeness of 82% in the redshift interval $2.9 < z < 4.5$. Increasing the cut on $\chi^2_{\rm star}$ forces quasars to be higher significance outliers from the stellar locus, thus decreasing the completeness. The decrease is particularly strong near $z \simeq 3.4$, because the stellar and quasar loci nearly overlap at this redshift (see Figure 4). Actually, the loci are still distinct in the ugr color–color diagram, but for fainter objects photometric errors blur this distinction because of low S/N in the u band. We choose $\chi^2_{\rm star} > 10$ (blue curves in Figure 5) as a compromise between completeness and the resulting efficiency of our search, which is quantified below.

Our binary quasar selection algorithm contains several steps. The area we consider for our search is the entire SDSS DR6 with an added constraint on galactic latitude $|b| > 25°$ to avoid contamination from highly reddened sources, resulting in a final survey area of 8142 deg^2. In this area, we first consider all objects that fulfill the set of conditions below to be photometric quasar candidates. In what follows we describe and motivate each criterion and parenthetically quote the resulting completeness, determined from our simulations ($i < 21$ and $2.9 < z < 4.5$), if each criterion is applied sequentially.

1. The image must be classified as STAR by the photometric pipeline (>99%).
2. Various cuts on flags produced by the SDSS photometric pipeline, similar to those used by spectroscopic quasar target selection (Richards et al. 2002b), must be satisfied (>99%).
3. The i-band photometric error must satisfy $\sigma_{\rm i} < 0.2$, excluding noisy data or spurious deblends (>99%).
4. The galactic extinction in the i band must be $A_{\rm i} < 0.3$ reducing contamination from highly reddened objects (>99%).
5. A photometric redshift dependent magnitude prior is imposed discarding stars which are stellar locus outliers but too bright to be quasars (99%).
6. Exclude objects with colors consistent with being white dwarf + M-star pairs (see Figure 4; Richards et al. 2001a), a significant contaminant (99%).
7. The apparent magnitude must satisfy $i < 21$ (96%).[15]
8. The $g-r$ color must be redward of the stellar locus in $g-r$ versus $r-i$ color–color diagram (see Figure 4) for $3.5 < z_{\rm phot} < 4.5$, significantly reducing contamination from faint red stars in this redshift range (92%).
9. Colors must be consistent with the quasar locus and have $\chi^2_{\rm phot} < 10$ (88%).
10. The photometric redshift must be in the range $2.85 < z_{\rm phot}$, thus excluding redshifts where selection is less efficient (see below, 82%).
11. Colors must be inconsistent with the stellar locus and have $\chi^2_{\rm star} > 10$ (64%).

Thus, our final completeness for selecting individual quasars with $i < 21$ and $2.9 < z < 4.5$ is 64%, with a redshift dependence given by the blue line in the left-hand panel of Figure 5. Our selection is much more efficient for brighter higher S/N sources since stellar locus outliers can be identified at higher statistical significance. The right panel of Figure 5 shows completeness as a function of redshift for varying limits on $\chi^2_{\rm star}$, but for brighter quasars with $i < 20.2$ satisfying the flux limit for the SDSS spectroscopic sample. The resulting completeness for $i < 20.2$ quasars is 83%, compared to 64% for the fainter $i < 21$ flux limit.

The efficiency of quasar targeting is another important criterion. Our spectroscopic follow-up (see Section 3.1) does not allow us to quantify this because we observed the best candidates first and our follow-up is far from complete. In principle, the efficiency could be computed if we knew the number densities of the contaminants on the sky. However, the number density of faint stars in the relevant regions of color space is not well constrained and is a strong function of Galactic latitude. Furthermore, faint red unresolved galaxies may also be a significant contaminant and estimating their number density is challenging. Instead, we obtain a rough estimate of the efficiency of our photometric quasar selection by comparing the number density of quasars predicted from the LF, to the total number of sources identified in our catalog.

[15] This reduction in completeness is due to Malmquist bias, given photometric errors.

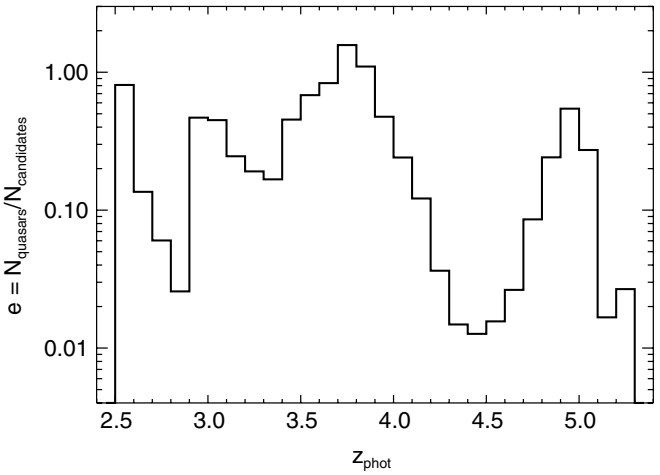

Figure 6. Estimated efficiency of the faint photometric quasar catalog as a function of redshift. The criteria in Section 2.5 have been applied, except that the photometric redshift range has been expanded to $2.5 < z_{\rm phot} < 5.3$. For $z \lesssim 4$, the selection efficiency is $\gtrsim$50%, except for dips at the problematic redshifts $z \sim 2.8$ and $z \sim 3.4$, where quasar colors intersect the stellar locus (see Figure 4). The efficiency reaches 1.6, and is thus unphysically above unity at $z_{\rm phot} \sim 3.8$, so we caution that our estimates are uncertain by at least this factor. For $z_{\rm phot} \gtrsim 4.2$, the efficiency drops precipitously, reaching a minimum of ∼1% at $z \sim 4.4$.

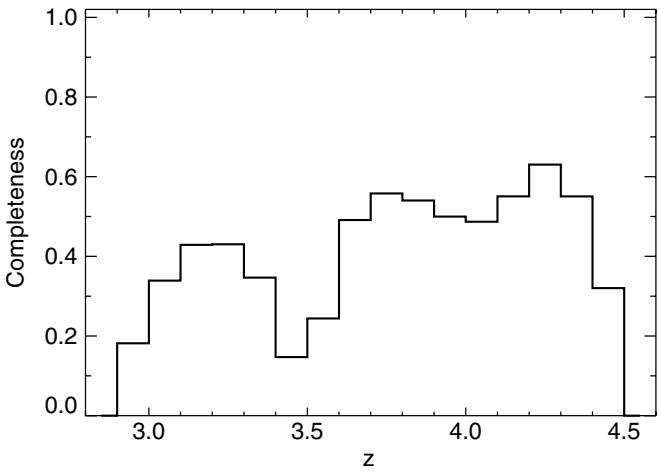

Figure 7. Completeness for photometrically selecting binary quasars as a function of redshift determined by applying the criteria in Section 2 ∼300,000 simulated binaries with $i < 21$.

Specifically, we use the LF (see discussion in Section 2.3) to compute the number counts of quasars in redshift bins, and multiply by the completeness determined from our simulations (see Figure 5), to determine the total number of quasars expected from our selection as a function of redshift, $N_{\rm QSO}(z)$. To mimic the effect of photometric redshift error, we convolve $N_{\rm QSO}(z)$ with a Gaussian with $\sigma_z = 0.16$, the standard deviation of our photometric redshifts for $z > 2.5$ (see Figure 2). Then, we can estimate the efficiency $e \equiv N_{\rm QSO}(z_{\rm phot})/N_{\rm candidates}(z_{\rm phot})$, which provides a rough estimate of the fraction of real quasars in our catalog as a function of photometric redshift.

The efficiency of our photometric catalog deduced in this way is shown in Figure 6. We have expanded the photometric redshift range of our selection to $2.5 \leqslant z_{\rm phot} \leqslant 5.3$ for this figure to illustrate the efficiency outside the limits of our survey ($2.9 < z < 4.5$), and to avoid edge effects in the photometric redshift convolution. Otherwise the criteria applied are exactly those in described in Section 2.5. For $z \lesssim 4$, the photometric selection efficiency is $\gtrsim$50%, except for dips at the problematic redshifts $z \sim 2.8$ and $z \sim 3.4$. The efficiency reaches 1.6, and is thus unphysically above unity at $z_{\rm phot} \sim 3.8$, so we caution that our estimates are uncertain by at least this factor. For $z_{\rm phot} \gtrsim 4.2$, the efficiency drops precipitously, reaching a minimum of ∼1% at $z \sim 4.4$. The contaminant at these redshifts is a rare population of red stars which have colors distinct from the stellar locus defined in Section 2.4.2 (see Figure 4), but which are significantly more abundant than high-redshift quasars. Because these red stars occur in much lower numbers than the stars on the stellar locus, they were not included in our parameterization in Section 2.4.

To improve the efficiency of our binary search, we compare candidates to the SDSS spectroscopic quasars, the FIRST radio survey (Becker et al. 1995), and the photometric KDE catalog (see Section 2.2 Richards et al. 2009), as we describe below.

2.6. Binary Quasar Selection

To select binary quasars, we first apply the cuts described in Section 2.5 to the SDSS photometric data to identify an initial photometric quasar catalog. We then search for pairs of objects in this catalog that satisfy the following additional criteria.

12. The angular separation must be $\Delta < 120''$, which projects to a comoving (proper) transverse distance of $R_\perp = 2.7\ h^{-1}$ Mpc (0.96 Mpc) and $R_\perp = 3.1\ h^{-1}$ Mpc (0.87 Mpc) at $z = 3$ and $z = 4$, respectively.
13. The quasar candidates must have similar photometric redshifts $\left|z_{\rm phot1} - z_{\rm phot2}\right| < 0.4$ (if applied to simulated quasar pairs ($2.9 < z < 4.5$) satisfying the criteria from 2.5 only 4% are rejected).
14. One member of the pair must either be: confirmed by the main SDSS spectroscopic survey to be a quasar at $z > 2.9$, or a FIRST radio source (Becker et al. 1995), or a member of the KDE photometric catalog (Richards et al. 2009).

In practice, the KDE completely dominates the auxiliary catalog criterion 14; the SDSS spectra and FIRST sources account for only ∼2% of matches. As we do not know the completeness of the KDE catalog to $i \sim 21$, we cannot precisely quantify how 14 impacts our overall completeness for selecting binaries, but this uncertainty has a very small effect, as we discuss in more detail below.

The completeness of the binary selection as a function of redshift is required for the clustering analysis in Paper II. For concreteness, consider the particular redshift range $z = 3.9$–4.0, where the completeness for selecting individual quasars is 77% (Figure 5). Without imposing criterion 14, the completeness for selecting binaries would be 53%, the square of the individual quasar completeness, but with a 4% reduction due to criterion 13. We naively guess that the combined KDE+ SDSS +FIRST sample has the same completeness as our photometric selection (for individual quasars) in this redshift bin. Then requiring that one member of each pair matches these auxiliary catalogs implies that we will recover $1-(1-0.77)^2 = 94\%$ of the binaries. Assuming the objects missed by our photometric selection and the auxiliary catalogs are uncorrelated, the total resulting completeness for binaries is 0.94×0.53 or 50%. More importantly, we do not need to characterize the KDE catalog very precisely, since even a ∼20% reduction in completeness (highly unlikely) would only amount to $\lesssim$10% error in characterizing our overall completeness for binaries. The other sources of statistical and systematic error in the clustering measurement in Paper II significantly overwhelm this conservative estimate of the error in

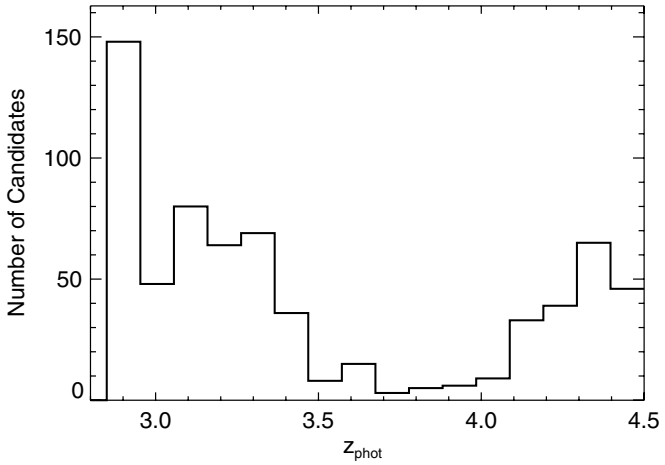

Figure 8. Distribution of photometric redshifts of both members of the 340 quasar pair candidates with $\theta < 60''$ selected by our survey.

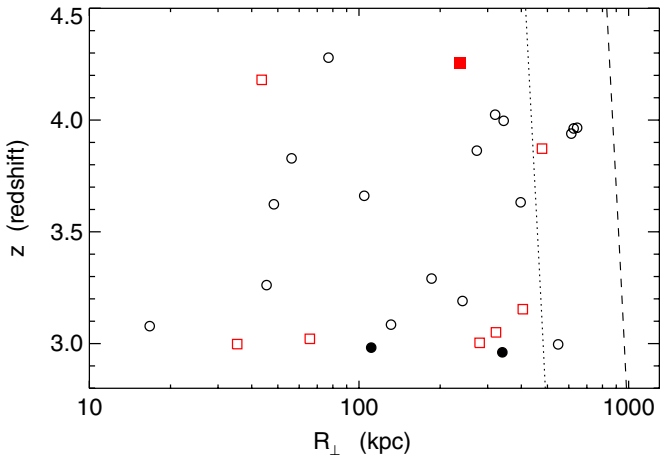

Figure 9. Distribution of redshift and proper transverse separation for 27 binary quasars in the SDSS imaging footprint. The (black) circles indicate the subset of objects which meet the selection criteria in Section 2, whereas the (red) squares do not. Previously known binaries are indicated by filled symbols. The dotted and dashed curves are the proper transverse distance corresponding to the fiber collision limit of the SDSS ($\theta = 55''$), and the angular separation limit of our binary search ($\theta = 120''$), respectively.

(A color version of this figure is available in the online journal.)

our completeness. Thus, we make the Ansatz that the auxiliary catalogs (KDE+ SDSS +FIRST) have the same completeness as our individual photometric quasar selection[16] (see Figure 5). Figure 7 shows the final completeness of our binary quasar selection as a function of redshift with this assumption.

2.7. Survey Status

Our sample of 27 $z > 2.9$ binaries (24 of them new discoveries) is presented in Section 4. Here, we discuss the status of spectroscopic follow-up observations of binary candidates in our survey. The redshift and angular distribution of our sample, shown in Figure 9, reflects specific biases in our follow-up observations. First, we tended to observe small separation pairs first, because they are more interesting for studies of the intervening intergalactic medium (IGM) and contribute more significantly to the quasar clustering signal (see Paper II). Thus, our follow-up is significantly less complete for larger splittings. As a result, we limit our clustering analysis in Paper II to $\theta < 60''$, and the status of our follow-up observations is quantified only for these separations. Of the 27 binaries in our sample, 22 have $\theta < 60''$, but only 15 of these satisfy the selection criteria laid out in Section 2 (the other seven were mostly discovered as pair candidates from the KDE catalog). The second noticeable trend in Figure 9 is that there are very few pairs with redshifts $z = 3.2$–3.5 and at $z > 4.1$. Figure 8 shows the distribution of mean photometric redshifts of the 340 (non-spurious) quasar pair candidates with $\theta < 60''$ selected by our survey. As expected, the largest number of candidates occur at redshifts where the efficiency is low in Figure 6, and thus at the corresponding redshifts we find fewer binaries in Figure 9, both because fewer candidates at these redshifts were targeted for follow-up spectroscopy and also the success rate is much lower.

We ran our binary selection on 8142 deg^2 of SDSS imaging, which resulted in 431 pair candidates with $\theta < 60''$. The SDSS images of all candidate quasar pairs were visually inspected to reject bad imaging data. The primary contaminants are regions around diffraction spikes from bright stars, challenging deblends, and fields containing a globular cluster where the stellar density is incredibly high. Of the 431 initial pair candidates, 91 were spurious, leaving 340 candidate quasar pairs. For some of the candidates, one member of the pair was observed by the SDSS spectroscopic survey and the spectra were examined in these cases to check for misidentifications; there were 21 objects which were not $z > 2.9$ quasars, leaving 319 candidates for follow-up. Color–color diagrams for each candidate were also inspected, and each candidate was assigned a rank (HIGH, MEDIUM, LOW) for follow-up observations. These rankings are subjective, reflecting the likelihood that the candidates were quasars based on their colors, the fidelity of the photometry (noisy data or suspicious deblends received a lower priority), and if both members were members of either the KDE, FIRST, or SDSS spectroscopic catalogs. In addition smaller separation pairs were given a higher priority.

The result of a successful spectroscopic follow-up observation of a quasar pair candidate falls into one of four categories: (1) a quasar–quasar pair at the same redshift, (2) a projected pair of quasars at different redshifts, (3) a quasar–non-quasar pair (i.e., either a star or a galaxy), (4) a pair of non-quasars. Of the 319 candidates for spectroscopic follow-up, 47 have one member confirmed to be a $z > 2.9$ quasar by SDSS spectroscopy and nine have one member in the FIRST catalog (which was not targeted by the SDSS spectroscopic survey). For only 37 of these 319 candidates are both objects members of the KDE catalog.

Table 1
Status of Quasar Pair Candidates with $\Delta\theta < 60''$

Status	$\bar{z}_{phot} < 3.5$	$\bar{z}_{phot} > 3.5$	Total
Observed	17	29	46
HIGH	28	27	55
MEDIUM	16	32	48
LOW	156	14	170
Total	217	102	319

Notes. The number of quasar pair candidates are listed and photometric redshifts of both members were averaged, allowing us to split the candidates into two redshift bins about $\bar{z}_{phot} = 3.5$. Binary candidates which were targeted for follow-up observations are labeled as "Observed." The remaining candidates have a priority of HIGH, MEDIUM, or LOW.

[16] We do not impose criterion 10 (see Section 2.5) in this estimate since no photometric redshift cuts were made on the KDE catalog.

Table 2
Binary Quasar Spectroscopy

Telescope	Instrument	Spectrograph Type	Spectral Coverage	FWHM	Dates	Reference
APO 3.5 m	DIS	Double	3800–10000	440/270	2005 Nov–Dec	...
MMT	Red channel	Single	5000–10000	1000	2006 Feb 19–21	...
MMT	Blue channel	Single	3200–8400	600	2006 Dec 13–15 and 2007 Mar 25	...
Palomar 200 inch	DBSP	Double	3100–9300	900/550	2007 Sep–2009 Apr	1
Mayall 4 m	RC-Spectrograph	Single	3600–9200	325	2008 Feb 9–11 and 2008 Jun 7–10	...
Keck II 10 m	ESI	Echellette	4000–10000	60	2006 Nov–2008 Jul	2

Notes. (1) Oke & Gunn 1982; (2) Sheinis et al. 2002.

The clustering analysis in Paper II splits our binary sample into two redshift bins ($2.9 < z < 3.5$ and $3.5 < z < 4.5$), and we describe the status of our follow-up observations similarly in bins of mean photometric redshift. Table 1 summarizes the status of all of the 319 candidates for spectroscopic follow-up. To date, our follow-up spectroscopy of binary candidates is about half finished, with 46 HIGH priority candidates observed and a total of 55 HIGH priority candidates remaining. Including the medium priority candidates in the tally implies we are only one third finished, but our experience is that these lower priority candidates have a much lower success rate. Of 170 LOW priority targets, 132 have one member with $z_{\rm phot} < 3.2$, indicating high contamination where the quasar and stellar loci cross at $z \sim 2.8$ (see Figures 4, 6, and 8). We caution that the fraction of candidates observed thus far is a poor predictor of the number of new binaries among our remaining targets, both because we observed the best candidates first and because the success rate for the lower priority candidates is unknown.

Indeed our tendency to observe the best candidates first is largely responsible for our high efficiency for finding binary quasars. Out of the 46 candidates observed to date with $\theta < 60''$, 16 were quasars at the same redshift: 15 correspond to binaries published in Table 3[17] and the other was the gravitational lens SDSS J1400+3134 at $z = 3.32$ (Inada et al. 2008). The remainder of our follow-up observations resulted in six projected quasar pairs, 15 quasar-non-quasar pairs, and nine pairs of non-quasars.

3. OBSERVATIONS

In this section, we describe the observations for our high-redshift binary survey. In Section 3.1, we discuss the follow-up spectroscopy of pair candidates and in Section 3.2 we explain our algorithm for estimating quasar systemic redshifts. As we elaborate below, optical spectra covering rest-frame ultraviolet emission lines yield quasar redshifts with large velocity uncertainties ($\sim$1000 km s^{-1}). Thus, redshifts estimation must be treated carefully in order to distinguish true binary quasars from projected pairs.

3.1. Spectroscopic Observations

Discovery spectra of our binary candidates were obtained with the Astrophysical Research Consortium 3.5 m telescope at the APO, the 6.5 m Multiple Mirror Telescope (MMT), the Palomar 200 inch telescope, and the Mayall 4 m telescope at Kitt Peak National Observatory. For the confirmation observations, we used low-resolution gratings and we typically oriented the slit at the position angle between the two quasars so that both members of the pair could be observed simultaneously. Exposure times varied with the telescope and observing conditions, but ranged from 600 s for the bright candidates on the larger telescopes to 2400 s for the faintest on the smaller telescopes. The relevant details of the confirmation observations are summarized in Table 2.

A subset of the confirmed binary quasars was later observed at higher resolution and S/N using the Echelle Spectrograph and Imager (ESI; Sheinis et al. 2002) on the Keck II 10 m telescope on Mauna Kea during a number of runs between 2006 November and 2008 July. The goal of the ESI observations was to measure small-scale transverse correlations of the Lyα forest and C IV metal line absorbers to reveal the small-scale structure of the IGM (Hennawi 2004; Ellison et al. 2007), characterize the size of metal-enriched regions (Ellison et al. 2007; C. L. Martin et al. 2010, in preparation), and constrain the dark energy density of the universe with the Lyα forest Alcock–Paczyński test (Alcock & Paczynski 1979; McDonald & Miralda-Escudé 1999; Hui et al. 1999; McDonald 2003). Our binary quasar search also uncovered many high-redshift projected pairs of quasars (see Section 2.7), which we also observed with ESI to study foreground quasar environments in absorption (Hennawi et al. 2006a; Hennawi & Prochaska 2007; Prochaska & Hennawi 2009) and the transverse proximity effect (e.g., Croft 2004; Kirkman & Tytler 2008).

ESI is an echellette spectrograph with 10 orders on the CCD, giving continuous spectral coverage from 4000 Å to 10000 Å. The resolving power is nearly constant across the orders. Our observations exclusively used the 1.″0 slit, resulting in a resolution of $R \simeq 5000$ or FWHM $\simeq$ 60 km s^{-1}. As the ESI slit is 20″ long, the instrument was rotated to observe both quasars simultaneously for pairs with $\Delta\theta \lesssim 15''$, whereas wider separation pairs were observed individually with the position angle set to the parallactic angle. The S/N of the resulting spectra vary, but typically peak at S/N $\sim$ 15–20 per pixel between the Lyα and C IV emission lines (around 7000 Å), with lower S/N at bluer and redder wavelengths. Total exposure times varied from 1 hr for our brighter targets to 6 hr for our faintest, with typical exposures around 2 hr.

The low-resolution discovery spectra and ESI spectra were reduced using the LowRedux[18] and ESIRedux[19] data reduction pipelines, respectively, written in the Interactive Data Language (IDL).

3.2. Estimating Systemic Redshifts

Quasar redshifts determined from the rest-frame ultraviolet emission lines (redshifted into the optical at $z \gtrsim 3$) can differ by over 1000 km s^{-1} from the systemic frame, because

[17] Note that only 15 of the total 27 binaries published in Table 3 satisfy both $\theta < 60''$ and the criteria in Sections 2.5 and 2.6.

[18] http://www.ucolick.org/~xavier/LowRedux/index.html

[19] http://www2.keck.hawaii.edu/inst/esi/ESIRedux/index.html

Table 3
High-redshift Binary Quasars in the SDSS Imaging Footprint

Name	R.A.	Decl.	u	g	r	i	z	$\chi^2_{\rm star}$	$\chi^2_{\rm phot}$	z	σ_z	Δv	$\Delta\theta$	$R_\perp$
SDSS J0004−0844A	00 04 50.674	−08 44 49.48	21.89	20.75	20.56	20.57	20.67	1.2	0.9	2.998	1450	650	4.4	35
SDSS J0004−0844B	00 04 50.920	−08 44 51.97	22.80	21.02	20.87	20.84	20.66	4.6	0.3	2.989	1450			
SDSS J0829+2927A	08 29 07.722	+29 27 54.71	23.64	20.93	20.28	19.68	19.30	63.3	22.5	3.054	1450	270	40.3	322
SDSS J0829+2927B	08 29 09.018	+29 27 18.10	22.04	20.07	19.95	19.83	19.88	36.8	1.2	3.050	710			
SDSS J0956+2643A	09 56 27.149	+26 43 24.47	21.61	19.43	19.22	19.28	19.30	143.2	2.6	3.087	520	150	16.5	131
SDSS J0956+2643B	09 56 25.934	+26 43 21.62	22.71	20.78	20.46	20.46	20.32	14.1	0.6	3.085	520			
SDSS J0959+1032A	09 59 03.843	+10 32 45.26	23.16	20.92	19.23	19.12	19.19	215.2	3.5	4.024	1450	250	44.1	320
SDSS J0959+1033B	09 59 05.139	+10 33 25.02	25.86	21.47	20.00	19.56	19.50	24.5	1.7	4.020	1500			
SDSS J1016+4040A	10 16 01.509	+40 40 52.89	21.26	19.42	19.22	19.10	18.84	109.8	8.1	2.996	520	1030	68.2	548
SDSS J1016+4040B	10 16 05.842	+40 40 05.80	22.12	20.36	20.06	20.10	19.92	49.7	1.8	2.983	1450			
SDSS J1021+1112A	10 21 16.982	+11 12 27.55	25.23	21.99	20.50	20.35	20.18	26.7	0.3	3.805	520	1470	7.6	56
SDSS J1021+1112B	10 21 16.468	+11 12 27.83	25.46	22.36	20.62	20.73	20.26	58.2	5.4	3.829	630			
SDSS J1053+5001A	10 53 20.150	+50 01 46.02	23.77	21.05	20.72	20.72	20.64	18.2	0.4	3.078	630	490	2.1	17
SDSS J1053+5001B	10 53 20.041	+50 01 47.84	23.35	21.10	20.84	20.88	21.02	19.4	1.5	3.085	520			
SDSS J1054+0215A	10 54 34.174	+02 15 51.95	23.03	20.22	18.69	18.61	18.75	244.9	6.2	3.984	630	1120	88.3	644
SDSS J1054+0216B	10 54 28.515	+02 16 16.37	23.21	20.58	19.41	19.10	18.97	12.9	5.3	3.966	790			
SDSS J1116+4118A	11 16 11.740	+41 18 21.51	20.30	18.49	18.13	17.93	17.95	87.0	6.0	2.982	520	1840	13.8	111
SDSS J1116+4118B	11 16 10.689	+41 18 14.44	21.29	19.41	19.14	19.01	19.02	87.9	1.7	3.006	520			
SDSS J1118+0202A	11 18 22.764	+02 02 36.35	24.82	21.13	19.81	19.77	19.86	75.0	0.8	3.939	790	0	83.8	613
SDSS J1118+0201B	11 18 17.920	+02 01 54.48	26.78	21.83	20.62	20.56	20.22	27.3	8.3	3.939	2000			
SDSS J1150+4659A	11 50 55.751	+46 59 41.96	22.43	20.52	20.34	20.56	20.16	66.7	12.2	3.005	710	140	34.9	280
SDSS J1150+4659B	11 50 52.353	+46 59 39.44	23.24	21.17	20.79	20.91	20.91	26.7	3.4	3.003	790			
SDSS J1159+3426A	11 59 06.632	+34 26 48.24	23.16	20.34	20.00	19.93	19.87	39.0	0.0	3.135	790	1340	51.2	405
SDSS J1159+3427B	11 59 02.974	+34 27 12.31	24.35	21.21	20.97	21.15	21.07	21.9	5.7	3.154	790			
SDSS J1248+1957A	12 48 46.012	+19 57 16.86	22.55	20.41	19.48	19.44	19.61	81.7	12.1	3.872	520	480	64.8	477
SDSS J1248+1956B	12 48 42.237	+19 56 39.90	24.39	21.75	20.16	20.01	20.10	91.8	1.2	3.864	520			
SDSS J1251+2715A	12 51 23.788	+27 15 24.61	23.14	21.29	20.29	20.21	20.02	19.7	5.0	3.660	1500	90	13.9	105
SDSS J1251+2715B	12 51 22.746	+27 15 23.60	23.22	21.82	20.78	20.68	20.57	14.6	3.5	3.661	1450			
SDSS J1307+0422A	13 07 56.734	+04 22 15.57	20.22	18.18	17.97	17.59	17.43	140.4	24.0	3.021	710	490	8.2	66
SDSS J1307+0422B	13 07 56.184	+04 22 15.50	21.41	19.68	19.25	19.02	19.12	18.3	9.1	3.028	710			
SDSS J1312+4616A	13 12 40.873	+46 16 47.86	25.60	21.78	20.18	19.86	19.46	49.7	8.4	3.971	1450	530	85.7	625
SDSS J1312+4615B	13 12 45.032	+46 15 33.85	25.03	22.17	20.43	20.25	20.31	99.8	1.7	3.963	2000			
PSSJ1315+2924A[a]	13 15 39.566	+29 24 40.76	23.00	21.53	19.71	19.33	19.35	113.4	3.4	4.18	2000	...	6.1	44
PSSJ1315+2924B[a]	13 15 39.122	+29 24 38.96	...	...	∼24	...	...	...	...	4.18	2000			
SDSS J1353+4852A	13 53 28.570	+48 52 34.06	24.65	21.71	20.40	20.40	20.18	62.7	1.9	3.863	520	1130	37.1	273
SDSS J1353+4853B	13 53 29.953	+48 53 08.53	25.23	21.93	20.88	20.86	20.81	23.7	1.4	3.845	520			
SDSS J1404+4005A	14 04 23.046	+40 05 11.03	24.07	20.90	19.57	19.29	19.22	68.5	1.6	3.999	1450	140	47.3	344
SDSS J1404+4005B	14 04 19.647	+40 05 37.79	24.98	22.47	20.97	20.50	20.47	18.8	1.1	3.997	630			
SDSS J1414+3955A	14 14 04.169	+39 55 43.54	20.73	18.72	18.57	18.64	18.58	264.8	3.1	3.218	520	1950	30.7	242
SDSS J1414+3955B	14 14 06.766	+39 55 36.27	24.39	21.31	20.90	20.86	20.93	24.1	1.3	3.191	520			
SDSS J1420+2831A	14 20 23.773	+28 31 06.57	25.43	22.18	20.30	19.93	19.63	60.8	3.3	4.305	710	1470	10.9	77
SDSS J1420+2830B	14 20 23.799	+28 30 55.72	23.13	23.13	20.73	20.22	20.08	65.2	5.1	4.279	790			
SDSS J1439−0033A	14 39 52.579	−00 33 59.08	25.14	23.11	20.79	20.44	20.22	53.6	3.2	4.255	0	170	33.4	237
SDSS J1439−0034B	14 39 51.600	−00 34 29.12	23.11	23.36	21.76	21.32	20.99	4.8	3.6	4.258	0			
SDSS J1541+2702A	15 41 10.367	+27 02 24.86	24.66	21.39	20.48	20.41	20.58	35.9	2.7	3.623	630	810	6.4	48
SDSS J1541+2702B	15 41 10.403	+27 02 31.22	23.47	21.51	20.42	20.42	20.44	52.6	4.6	3.636	520			
SDSS J1546+5134A	15 46 14.229	+51 34 05.00	20.68	19.39	19.09	18.93	18.81	11.5	5.4	2.961	1450	1240	42.2	340
SDSS J1546+5134B	15 46 10.538	+51 34 29.44	22.17	20.49	20.31	20.25	20.63	31.4	4.8	2.944	650			
SDSS J1622+0702A	16 22 10.109	+07 02 15.34	21.76	17.43	17.03	16.85	16.82	849.0	1.7	3.264	790	160	5.8	45
SDSS J1622+0702B	16 22 09.815	+07 02 11.53	25.60	20.68	20.16	20.03	20.02	31.7	1.7	3.262	630			
SDSS J1626+0904A	16 26 42.067	+09 04 37.35	25.42	21.46	20.50	20.49	20.37	23.7	2.4	3.632	1450	450	52.7	398
SDSS J1626+0904B	16 26 38.623	+09 04 24.20	25.03	21.67	20.74	20.68	20.95	18.6	2.8	3.639	1450			
SDSS J1630+1152A	16 30 55.956	+11 52 29.43	21.80	19.33	18.93	18.71	18.66	71.2	4.4	3.277	1450	970	23.8	186
SDSS J1630+1152B	16 30 56.727	+11 52 50.34	26.36	20.63	20.31	20.35	20.12	81.7	8.0	3.291	790			

Notes. Units of right ascension are hours, minutes, and seconds, and units of declination are degrees, arcminutes, and arcseconds. The brightest member of the pair in the i band is always labeled "A" and the fainter member is labeled "B." Extinction-corrected SDSS five-band point-spread function (PSF) photometry is given in the columns u, g, r, i, and z. The minimum stellar locus and quasar locus distances are denoted by the columns labeled $\chi^2_{\rm star}$ and $\chi^2_{\rm phot}$, respectively. The redshifts are indicated by the column labeled z, σ_z is our estimate of the redshift uncertainty in km s^{-1}, and Δv is the velocity difference between the two members of a pair in km s^{-1}. The column labeled $\Delta\theta$ is the angular separation in arcseconds and $R_\perp$ is the transverse proper separation in kpc. Note that z denotes the z-band magnitude, whereas z indicates redshift. [a] This quasar pair was selected via a different method during a pilot search for proto-clusters associated with $z > 4$ quasars (see Section 4.1). The redshifts quoted are approximate and we did not measure a velocity difference. The fainter quasar PSS 1315+2924B is not detected in the SDSS imaging, its quoted r-band magnitude quoted is an estimate from Keck LRIS R-band imaging.

of outflowing/inflowing material in the broad line regions of quasars (Gaskell 1982; Tytler & Fan 1992; Vanden Berk et al. 2001; Richards et al. 2002a; Shen et al. 2008b). A redshift determined from the narrow forbidden emission lines, such as [O III] λ5007, or Balmer lines such as Hα λ6563 are much better predictors of systemic redshift (Boroson 2005), but at $z \gtrsim 3$, spectral coverage of these lines would require observations in the near-infrared. Instead, we follow the approach described in Shen et al. (2007), and determine the redshifts of quasars from our optical spectra. Shen et al. (2007) measured the correlation between the relative shifts of the high-ionization emission lines Si IV, C IV, C III, and the shift between these respective lines and the systemic frame, as traced (approximately) by the Mg II line (Richards et al. 2002a). These correlations can then be used to estimate the systemic redshift and the associated error, from high-ionization line centers. As an operational definition, we consider quasar pairs with velocity differences of $|\Delta v| \leqslant 2000$ km s^{-1} to be at the same redshift, since this brackets the range of velocity differences caused by both peculiar velocities, which could be as large as ∼500 km s^{-1} if binary quasars reside in rich environments, and systemic redshift uncertainties, which can be larger than ∼1000 km s^{-1}.

Our quasar spectra come from a variety of instruments (see Table 2) and have varying S/Ns and spectral coverage. The ESI spectra are always used for redshift determination when available, otherwise we use SDSS spectra or the low S/N discovery spectra. For noisy spectra which can have intrinsic absorption features, flux-weighted centering often yields erroneous results for emission line centers. For this reason, we adopt the more robust line-centering procedure introduced in Hennawi et al. (2006a), and used by Shen et al. (2007). For those spectra where prominent UV emission lines cannot be centered because of low S/N, limited spectral coverage, or strong intrinsic absorption features, the redshift is measured using the peak of the Lyα emission line measured after smoothing with a 1000 km s^{-1} boxcar. A shift is then applied between the Lyα redshift and the systemic frame, which was measured on average by Shen et al. (2007).

4. THE BINARY QUASAR SAMPLE

We present a sample of 24 new high redshift, $2.9 \lesssim z \lesssim 4.3$, binary quasars with (proper) transverse separations 10 kpc $< R_\perp <$ 650 kpc. Eight members of this sample are very close binaries with $R_\perp <$ 100 kpc, and four of these are at $z > 3.5$. Table 3 lists relevant quantities for a total of 27 binaries in the SDSS imaging area footprint, including three previously known pairs. These are SDSS J1116+4118 and SDSS J1546+5134, which were published in Hennawi et al. (2006b), and SDSS J1439−0033, discovered serendipitously by Schneider et al. (2000). Of this sample of binaries, 22 of 27 have angular separations $\theta \leqslant 55''$, below the SDSS fiber collision scale. For two of the binaries both objects were observed by the SDSS spectroscopic survey: SDSS J1016+4040 has angular separation $\theta = 68\farcs2$, i.e., larger than the fiber collision limit, and SDSS J1116+4118 ($\theta = 13\farcs8$) was observed by overlapping spectroscopic plates (Hennawi et al. 2006b).

Several of the binary quasars listed in Table 3 do not meet all of the criteria laid out in Section 2. As we describe further below, PSS 1315+2924, one of the closest systems in our sample, was selected by a different method altogether as its faint companion is not even detected in the SDSS imaging data. The remaining binaries which fail to meet these criteria are SDSS J0004−0844, SDSS J0829+2927, SDSS J1150+4659, SDSS J1159+3426, SDSS J1248+1957, and SDSS J1307+0422, as well as SDSS J1439−0033 discovered by Schneider et al. (2000). Many of these objects were targeted for follow-up because they were pair candidates in the KDE photometric catalog. In Paper II, we restrict the clustering analysis to the subset of pairs which meet the selection criteria in Section 2, for which we calibrated the completeness of our search.

The distribution of redshifts and proper transverse separations probed by the 27 binary quasars in the SDSS footprint is illustrated by the scatter plot in Figure 9. The relative paucity of pairs with $\theta \gtrsim 60''$ results from the incompleteness of our spectroscopic follow-up campaign. The lack of pairs with $z = 3.2$–3.5 and at $z > 4.1$ occurs because photometric quasar selection is inefficient at these redshifts (see discussion in Section 2.7).

Spectra of selected members of our binary sample are shown in Figures 10 ($2.9 < z < 3.5$) and 11 ($z > 3.5$). All of the spectra in these figures are from ESI with the exception of SDSS J1116+4118, for which we show the SDSS spectra.

4.1. The Discovery of PSS 1315+2924

The faint quasar companion to the bright quasar PSS 1315+2924 was discovered during a pilot search for proto-clusters associated with $z > 4$ quasars (Djorgovski 1999; Djorgovski et al. 1999). Two different strategies were employed in this search. In the first, *R*-band snapshot images were taken of about twenty $z \sim 4$ quasars to moderate depth $R \lesssim 25$ using the Low Resolution Imaging Spectrograph (LRIS; Oke et al. 1995) on the Keck I telescope. If a companion was found within ∼10″ of the quasar it was spectroscopically observed with LRIS in long-slit mode. For the second approach, deep imaging was obtained in the BRI filters ($R \lesssim 26$) for a sample of about 10 $z \sim 4$ quasars, again using LRIS. Color selection was used to search for dropout candidates (at these redshifts, the continuum drop is dominated by the Lyα forest, rather than the Lyman break, which is used to select galaxies at $z \sim 2$–3.5). These candidates were then followed up with multislit spectroscopy using LRIS in spectroscopic mode. The faint $R \simeq 24.1$ companion PSS 1315+2924B (see Table 3) was found from this color-selection approach, and spectra of both quasars were obtained on 1999 April 14 UT with LRIS, and reduced using standard techniques. In addition, this protocluster survey uncovered about two dozen star-forming galaxies at small angular separations $\theta \lesssim 10''$ from the quasars. A similar survey was also carried out around $z \sim 5$–6 quasars, which led to the discovery of a companion $z = 5.02$ quasar 196″ away from a high-redshift quasar at $z = 4.96$ (Djorgovski et al. 2003).

4.2. Contamination by Gravitational Lenses

It is possible that some of the quasar pairs with image splittings $\lesssim 20''$ in our sample are wide-separation strong gravitational lenses rather than binary quasars. Indeed, several gravitationally lensed quasars with image splittings $\theta \gtrsim 3''$ have been discovered in the SDSS (Inada et al. 2003, 2008; Oguri et al. 2004, 2005). In particular, our binary search recovered one of the high-redshift gravitational lenses from the sample of Inada et al. (2008), SDSS J1400+3134 at $z = 3.32$ with image splitting $\theta = 1\farcs7$. The largest separation lens discovered to date is the $z = 2.2$ quasar lensed into two images separated by $22\farcs5$ by a foreground cluster (Inada et al. 2006). But the lower number density of $z > 3$ quasars makes high-redshift wide-separation lenses correspondingly rarer than at

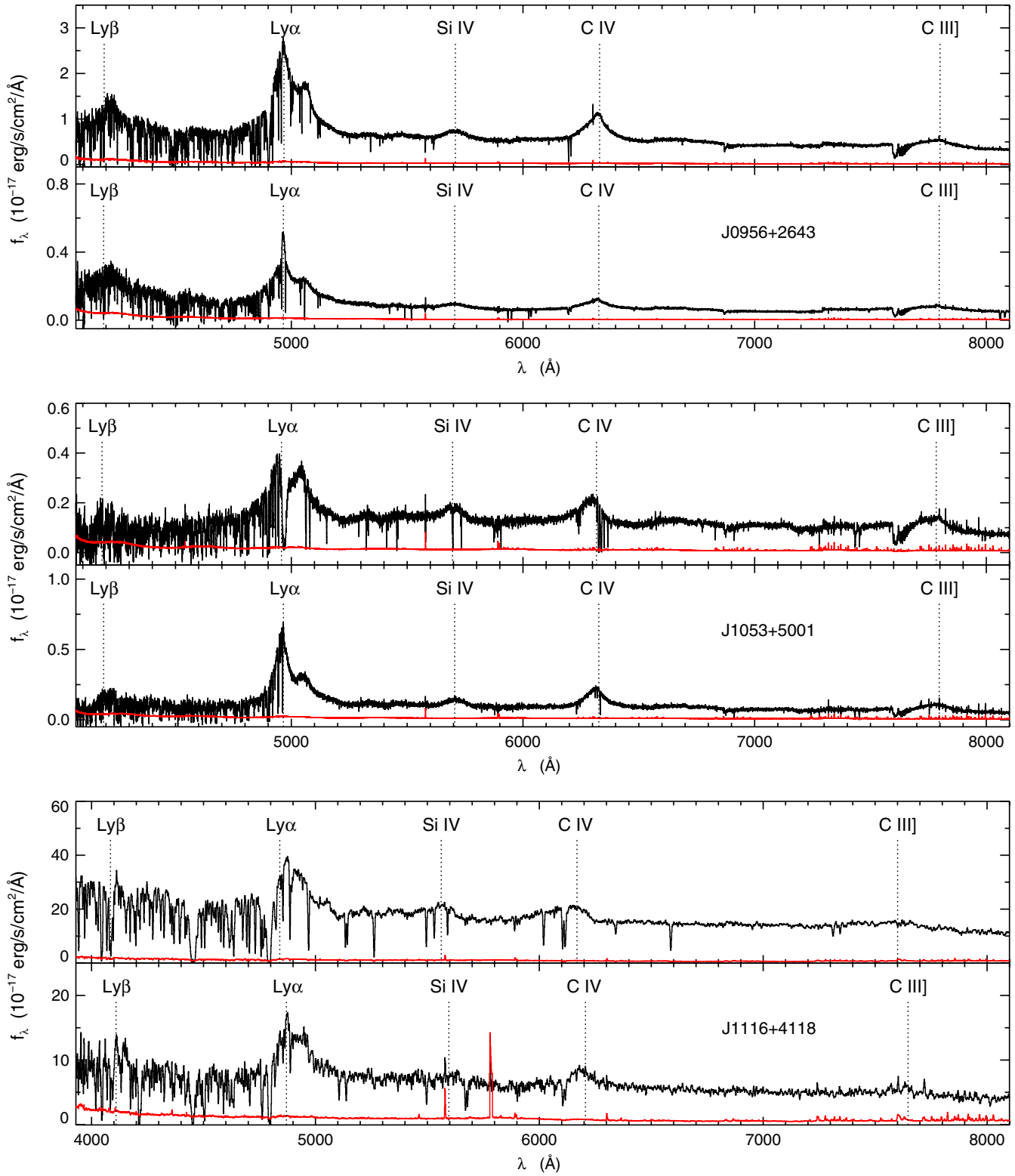

Figure 10. Spectra of selected binary quasars in the redshift range $2.9 < z < 3.5$. A three pixel boxcar smoothing has been applied to all spectra. The red curves indicate the 1σ error array. Object "A" is always shown in the top panel of each plot. All spectra are from ESI with the exception of SDSS J1116+4118, for which we show the SDSS spectra. The strong features in the ESI spectra at 7600 Å are atmospheric telluric absorption.

(A color version of this figure is available in the online journal.)

$z \sim 2$. Using cosmological ray-tracing simulations, Hennawi et al. (2007a) determined that a quasar sample with the flux limit of our search should contain ∼2 lenses with image splitting $\theta > 10''$ and $z > 3$. However, this estimate is extremely sensitive to the assumed value of σ_8 (Li et al. 2006, 2007), which was high ($\sigma_8 = 0.95$) for the Hennawi et al. (2007a) study; the expectation for high-redshift lenses is therefore lower by a factor of $\gtrsim$5 (Li et al. 2007) if one adopts the lower value of

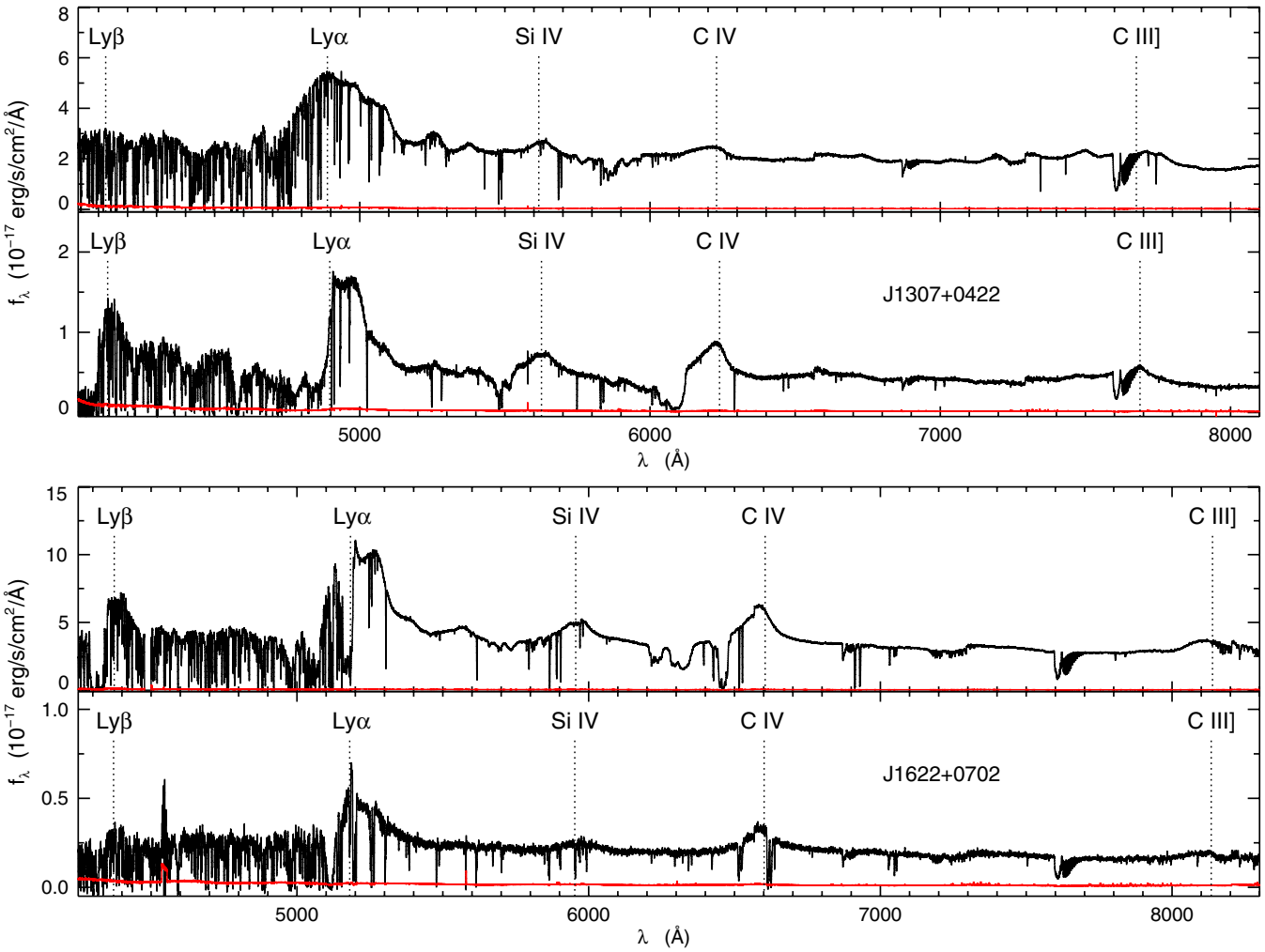

Figure 10. (Continued)

$\sigma_8 = 0.80$ favored by the *WMAP* five-year data (Dunkley et al. 2009).

A quasar pair can be positively confirmed as a binary if the spectra of the images are vastly different (cf. Gregg et al. 2002), if only one of the images is radio-loud (an O^2R pair, in the notation of Kochanek et al. 1999), or if the quasars' hosts are detected and they are not clearly lensed. The sufficient conditions for a pair to be identified as a lens are the presence of more than two images in a lensing configuration, the measurement of a time delay between images, the detection of a plausible deflector, or the detection of lensed host galaxy emission (see, e.g., Kochanek et al. 1999; Mortlock et al. 1999).

The sample of binaries in Table 3 contains 10 systems with $\theta < 20''$ which we consider as potential lenses. We have ESI spectra of all but two of these, SDSS J0004−0844[20] and PSSJ1315+2924. For all cases with ESI spectra, we can convincingly rule out the lensing hypothesis because of their spectral dissimilarity (see Figures 10 and 11). In addition, SDSS J1307+0422A was detected in the FIRST survey with 20 cm flux $F_A = 14.3$ mJy. Using *i*-band apparent magnitudes to compute a flux ratio implies the flux of the second image would be $F_B = 3.8$ mJy under the lensing hypothesis. This is four times brighter than the FIRST flux limit, however, no radio counterpart is detected.[21]

For both SDSS J0004−0844 ($z = 3.00$, $\theta = 4\farcs4$) and PSSJ1315+2924 ($z = 4.18$, $\theta = 6\farcs1$) we have obtained deep imaging using the LRIS (Oke et al. 1995) on the Keck I telescope. For SDSS J0004−0844 our LRIS *R*-band image reaches an approximate point source depth of $R \sim 24$, and there is no evidence for a lensing galaxy or cluster. Our LRIS image of PSSJ1315+2924 reaches a depth of $R \sim 26$, and there is similarly no evidence for a lens. Although the *absence* of a deflector in images of a quasar pair does not strictly speaking confirm the binary hypothesis, it makes it very likely. For wide-separation lenses with $\Delta\theta \gtrsim 3''$, such as SDSS J1004+4112 ($\Delta\theta_{\rm max} = 14\farcs62$, $z_{\rm lens} = 0.68$), Q 0957+561 ($\Delta\theta = 6\farcs2$, $z_{\rm lens} = 0.36$; Walsh et al. 1979), or SDSS J1029+2623 ($\Delta\theta_{\rm max} = 22\farcs5$, $z_{\rm lens} \sim 0.6$) where the lens is a bright galaxy in a cluster or group, the lens galaxies would have $r \sim 20$–21 at the most probable redshifts of $z = 0.3$–0.7 (Hennawi et al. 2007a), and would thus be easily detectable in our LRIS images. Although we cannot completely rule out lenses with $z \gtrsim 1$, a wide-separation $z > 3$ quasar lensed by such a high-redshift group or

[20] A spectrum of SDSS J0004−0844 was obtained the Magellan Echellette (MagE) Spectrograph on the Magellan Clay Telescope. These data are not published here, but the different Lyα emission line profiles also allow us to compellingly argue against gravitational lensing.

[21] Although the optical flux ratio could be anomalous relative to the radio because of microlensing, anomalies as large as a factor of ∼4 are rare (e.g., Pooley et al. 2007).

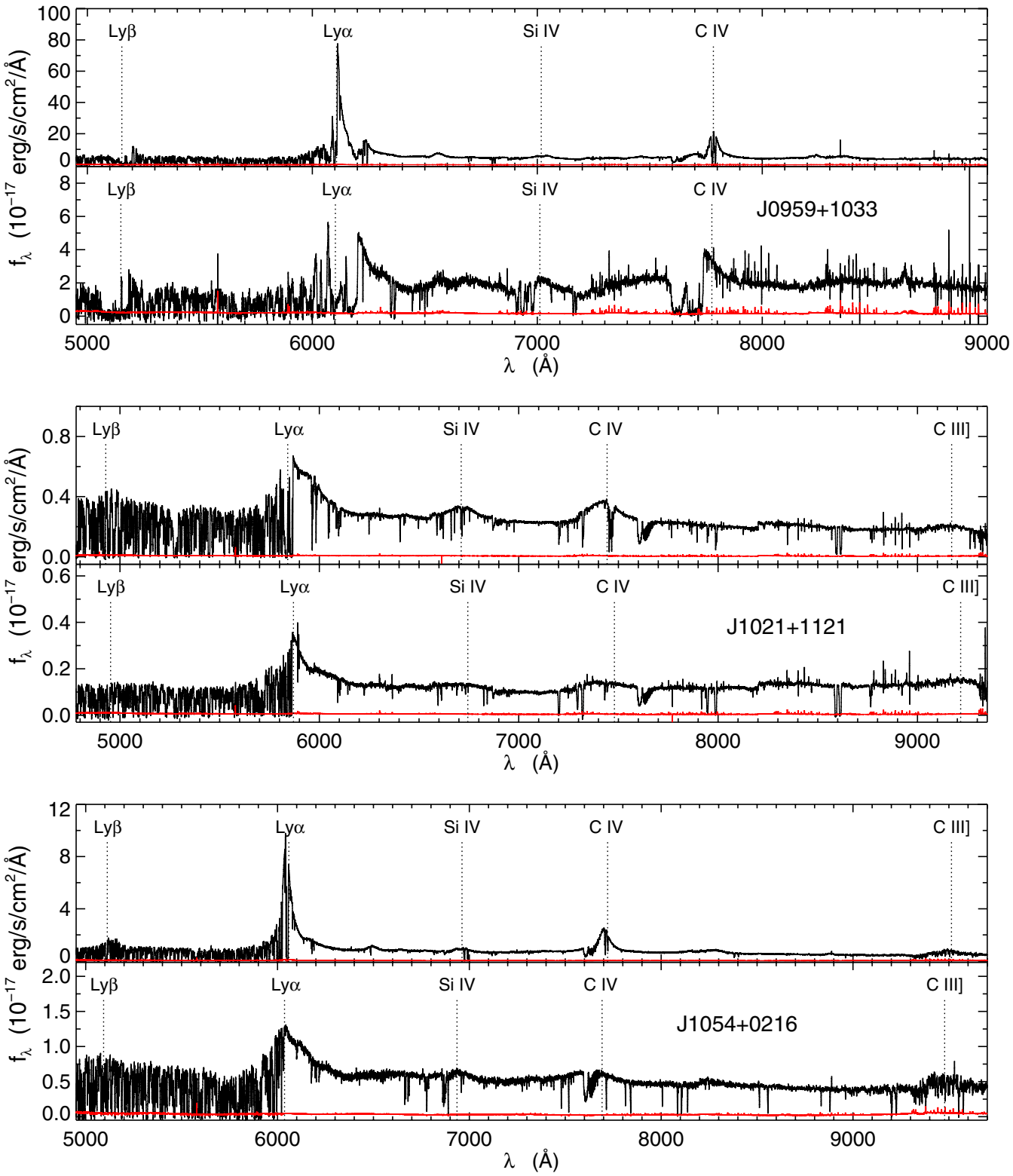

Figure 11. Same as Figure 10 but for binary quasars with $z > 3.5$.
(A color version of this figure is available in the online journal.)

cluster is extremely unlikely because structures with appreciable strong-lensing cross section are predicted to be extremely rare at $z > 1$ (Hennawi et al. 2007a, 2007b). Thus, we are confident that all of the quasar pairs in our sample are indeed binary quasars.

5. SUMMARY AND CONCLUSIONS

We have conducted the first systematic survey to discover high-redshift binary quasars. Using color-selection and photometric redshift techniques, we mined 8142 deg^2 of SDSS

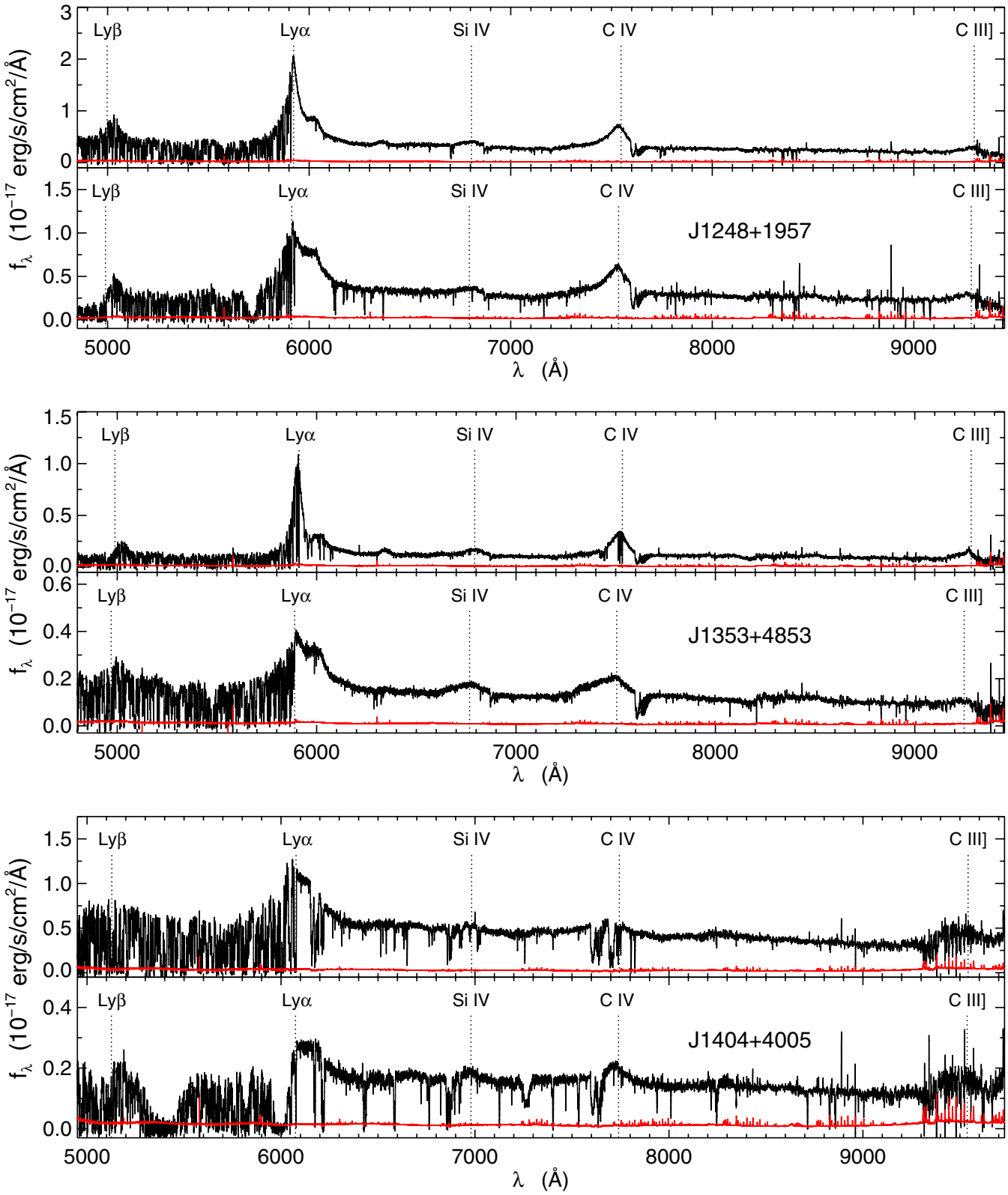

Figure 11. (Continued)

imaging data for binary quasar candidates, and confirmed them spectroscopically with follow-up observations on 4 m class telescopes. Our sample of 24 new binaries at redshifts $2.9 \lesssim z \lesssim 4.3$ with (proper) transverse separations 10 kpc $< R_\perp <$ 650 kpc increases the number of such objects known by an order of magnitude. Eight members of this sample are very close pairs with $R_\perp < 100$ kpc, and of these close systems four are at $z > 3.5$. More importantly, whereas the only previously known close binary at $z \sim 4$ was discovered serendipitously (Schneider et al. 2000), we defined an algorithm for homogeneously selecting binary candidates and quantified its completeness and efficiency using simulations.

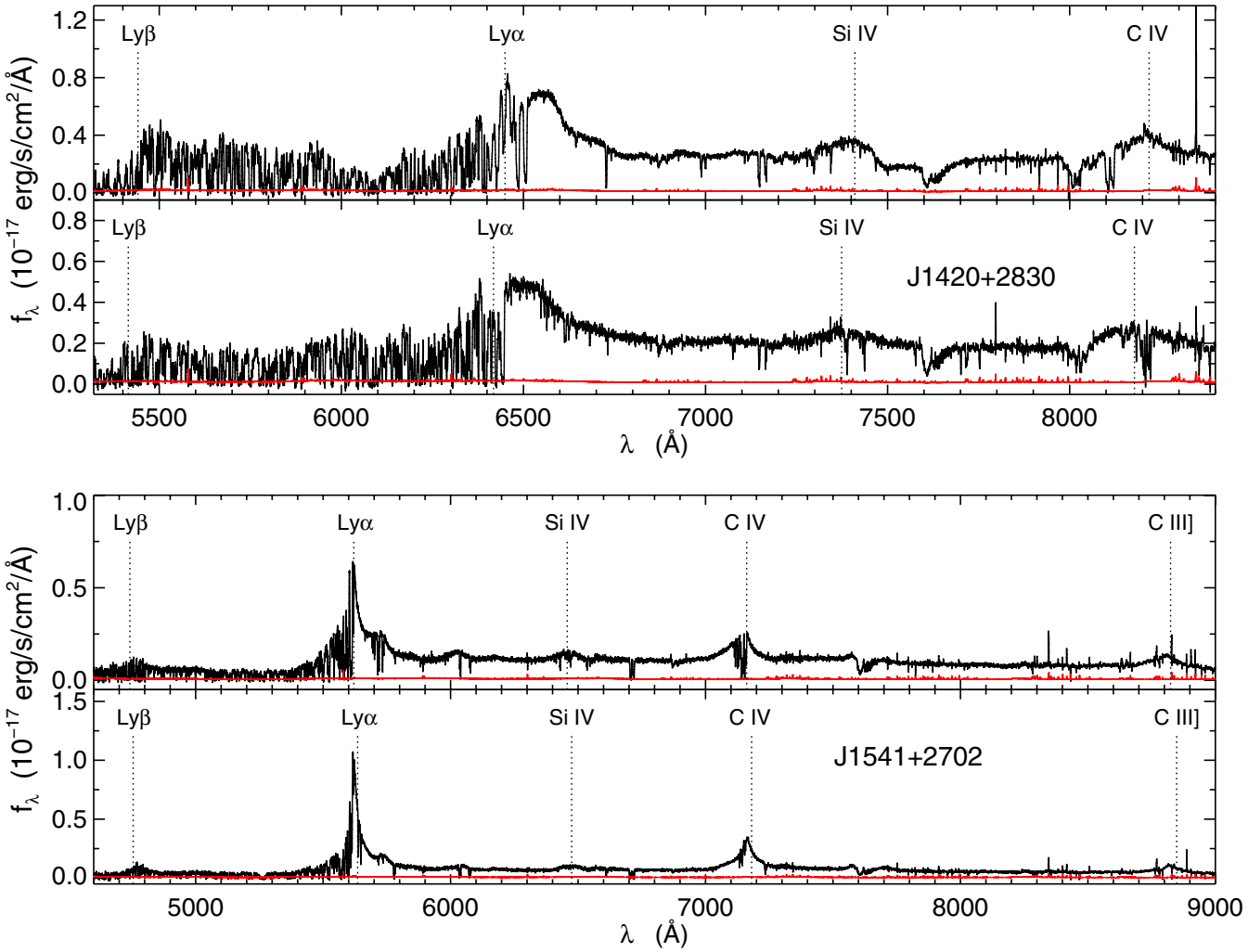

Figure 11. (Continued)

Armed with this new sample of binaries and a well-understood selection function, Paper II presents the first measurement of the small-scale clustering ($R < 1\ h^{-1}$ Mpc comoving) of high-redshift quasars. On large scales, high-redshift quasars cluster much more strongly than their low-redshift counterparts (Shen et al. 2007), indicating that quasars are hosted by extremely massive dark matter halos ($M \gtrsim 10^{13}\ h^{-1}\ M_{\odot}$)—perhaps not so surprising as these quasars likely harbor the most extreme black holes ($M \gtrsim 10^{9}\ M_{\odot}$) in the universe (e.g., Shen et al. 2008b). Small-scale clustering measurements characterize the 10 kpc–1 Mpc scale environments of these extreme black holes, providing important clues about how quasar activity is triggered (Thacker et al. 2006, 2008; Hopkins et al. 2008; Wetzel et al. 2009b) and constraining how quasars populate their dark matter halos (Wetzel et al. 2009b; Bonoli et al. 2010). Because our survey is only about half-complete, we can only place lower limits on the small-scale clustering. Nevertheless, even these lower limits provide important constraints on models (see Paper II).

The massive dark halos inhabited by high-redshift quasars (Shen et al. 2008b) suggest that high-redshift binaries represent exponentially rare conjunction of two extremely massive black holes (and possibly two dark matter halos). Furthermore, the simultaneity of their luminous quasar phases is another important coincidence. Using the LF and the number of binaries detected in our survey, we can estimate the fraction of quasars which have an active companion. In the redshift range $3.5 < z < 4.5$, there are $N_{\rm QSO}(i < 21) = 1.9\ {\rm deg}^{-2}$, or about ∼15,000 in the SDSS area we surveyed. We uncovered four binary quasars with $R < 100$ kpc ($\theta \lesssim 15''$) and $i < 21$, which given our incompleteness (see Figure 7), implies ∼8 binaries actually exist. Thus, the companion probability is extremely small ∼0.05%. Equivalently, over this redshift range our survey volume is ∼100 Gpc^3 (comoving), implying a comoving number density $n_{\rm binary} \sim 10^{-10}$ Mpc^{-3}, or about one binary per 10 Gpc^3. For comparison, this is an order of magnitude rarer than the extremely rare $z \sim 6$ quasars (Fan et al. 2001), and corresponds to a volume 30 times larger than the Millennium Simulation (Springel et al. 2005). Despite their paucity, the handful of binaries presented here amount to a substantial small-scale clustering signal (Shen et al. 2010): although the observed pair fraction is incredibly low, the probability of such associations occurring at random is orders of magnitude lower.

Binaries are scarce in our survey partly because at $z = 4$, $i < 21$ corresponds to an extremely luminous (and therefore rare) quasar, $M_i < -26.5$,[22] i.e., comparable to 3C 273 and about ∼3.5 mag brighter than the canonical distinction ($M_{\rm B} < -23$) between quasars and Seyferts. Upcoming deep

[22] Following Richards et al. (2006), we quote i-band absolute magnitudes K-corrected to $z = 2$.

synoptic surveys such as the Panoramic Survey Telescope & Rapid Response System (Pan-STARRS; Kaiser et al. 2002) and the Large Synoptic Survey Telescope (LSST; Ivezic et al. 2008), will combine variability and color selection to identify large photometric samples of faint quasars with high completeness and efficiency. The number of binaries uncovered by these surveys scales as $N \propto N_{\rm QSO}^2 A$, where $N_{\rm QSO}$ is the quasar number counts and A is the survey area. Extrapolating our LF to $i < 24.5$ (i.e., $M_i < -23$ at $z = 4$), we find $N_{\rm QSO}(i < 24.5) \simeq 30$ deg^{-2} for $3.5 < z < 4.5$, or about 15 times the number density of the SDSS in this range. The LSST will discover all active galaxies over 20,000 deg^{-2} even beyond this depth, implying a factor of ∼600 increase in the number of quasar pairs. If we naively assume clustering is independent of luminosity[23] and extrapolate from the size of our sample, we predict ∼5000 binary quasars with $R \lesssim 100$ kpc and $3.5 < z < 4.5$ in the LSST imaging. The shallower ($i < 24$) but wider ($A = 3\pi$) Pan-STARRS1 survey will contain a comparable number. The clustering measurement errors scale as the square root of the number of binaries, implying errors about 25 times smaller than achieved in (Shen et al. 2010) from our sample. Furthermore, the fainter sample and dramatically improved statistics will allow a precise investigation of the redshift and luminosity dependence of both small- and large-scale clustering, resulting in powerful constraints on clustering models.

Searching for galaxy overdensities around the binaries published here will shed light on their environments and the mechanism triggering their quasar activity. Although the separations of our binary quasars are too large for direct gravitational interactions to trigger accretion, they could reside in the same overdense environments whereby interactions with other galaxies make quasar activity more likely (e.g., Djorgovski 1991; Hopkins et al. 2008). The idea of using quasars as beacons to pinpoint dense regions in the early universe is not new (e.g., Djorgovski 1999; Djorgovski et al. 1999). Deep imaging studies of high-redshift quasar environments in search of overdensities and protoclusters have been conducted at $z \sim 3$ (e.g., Steidel et al. 1999; Infante et al. 2003), by Djorgovski and collaborators at $z \sim 4$ (Djorgovski 1999; Djorgovski et al. 1999, 2003), and by several groups at $z \sim 5$–6, (Stiavelli et al. 2005; Zheng et al. 2006; Kashikawa et al. 2007; Kim et al. 2009; Priddey et al. 2008). While it is still unclear whether high-redshift quasars reside in protoclusters, compelling evidence for overdensities has been found around a handful of $z > 4$ radio galaxies (e.g., Venemans et al. 2002, 2004; Miley et al. 2004; Overzier et al. 2006, 2008; Venemans et al. 2007). If similar deep imaging and multi-object spectroscopy of our high-redshift binaries uncovers protocluster environments, this would establish that either the binaries are the highest sigma peaks in the early universe, or that enhanced quasar activity is triggered by galaxy interactions. Furthermore, the kinematics and size of such an overdensity could distinguish these alternatives. Intriguingly, Fukugita et al. (2004) obtained deep Subaru images of the $z = 4.25$ quasar pair discovered by Schneider et al. (2000) and found no evidence for an overdensity of galaxies. But the tenfold increase in high-redshift binaries published here provides ample opportunity for future detailed statistical studies.

We conclude with the reminder that our survey for quasar pairs is ongoing and less than 50% complete. Although the binary yield will likely drop because we observed the best candidates first, we anticipate discovering 10–20 more high-redshift binaries in the SDSS imaging.

We acknowledge helpful discussions with J. Cohn, N. Padmanabhan, D. Schlegel, D. Weinberg, A. Wetzel, and M. White. For part of this work, J.F.H. was supported by a NASA Hubble Fellowship grant no. 01172.01-A and by the NSF Postdoctoral Fellowship program (AST-0702879). Y.S. and M.S. acknowledge support from the National Science Foundation (NSF) (AST-0707266). D.P.S. similarly acknowledges support from the NSF (AST-0607634). S.G.D., A.A.M., and E.G. acknowledge partial support from the NSF grant AST-0407448 and from the Ajax Foundation. C.L.M. acknowledges support from the Packard Foundation and the NSF (AST-0808161).

Funding for the SDSS and SDSS-II has been provided by the Alfred P. Sloan Foundation, the Participating Institutions, the National Science Foundation, the U.S. Department of Energy, the National Aeronautics and Space Administration, the Japanese Monbukagakusho, the Max Planck Society, and the Higher Education Funding Council for England. The SDSS Web Site is http://www.sdss.org/.

The SDSS is managed by the Astrophysical Research Consortium for the Participating Institutions. The Participating Institutions are the American Museum of Natural History, Astrophysical Institute Potsdam, University of Basel, University of Cambridge, Case Western Reserve University, University of Chicago, Drexel University, Fermilab, the Institute for Advanced Study, the Japan Participation Group, Johns Hopkins University, the Joint Institute for Nuclear Astrophysics, the Kavli Institute for Particle Astrophysics and Cosmology, the Korean Scientist Group, the Chinese Academy of Sciences (LAMOST), Los Alamos National Laboratory, the Max-Planck-Institute for Astronomy (MPIA), the Max-Planck-Institute for Astrophysics (MPA), New Mexico State University, Ohio State University, University of Pittsburgh, University of Portsmouth, Princeton University, the United States Naval Observatory, and the University of Washington.

Some of the data presented herein were obtained at the W.M. Keck Observatory, which is operated as a scientific partnership among the California Institute of Technology, the University of California and the National Aeronautics and Space Administration. The Observatory was made possible by the generous financial support of the W.M. Keck Foundation. The authors recognize and acknowledge the very significant cultural role and reverence that the summit of Mauna Kea has always had within the indigenous Hawaiian community. We are most fortunate to have the opportunity to conduct observations from this mountain.

[23] The luminosity dependence of large-scale quasar clustering at high redshift has yet to be quantified, although there is tentative evidence that the brightest quasars cluster more strongly at $z \lesssim 2$ (Paper II).

REFERENCES

Abazajian, K., et al. 2003, AJ, 126, 2081
Abazajian, K., et al. 2004, AJ, 128, 502
Abazajian, K., et al. 2005, AJ, 129, 1755
Adelberger, K. L., & Steidel, C. C. 2005a, ApJ, 630, 50
Adelberger, K. L., & Steidel, C. C. 2005b, ApJ, 627, L1
Adelman-McCarthy, J. K., et al. 2006, ApJS, 162, 38
Adelman-McCarthy, J. K., et al. 2007, ApJS, 172, 634
Adelman-McCarthy, J. K., et al. 2008, ApJS, 175, 297
Alcock, C., & Paczynski, B. 1979, Nature, 281, 358
Bahcall, J. N., Kirhakos, S., Saxe, D. H., & Schneider, D. P. 1997, ApJ, 479, 642
Barnes, J. E., & Hernquist, L. 1996, ApJ, 471, 115
Becker, R. H., White, R. L., & Helfand, D. J. 1995, ApJ, 450, 559

Blanton, M. R., Lin, H., Lupton, R. H., Maley, F. M., Young, N., Zehavi, I., & Loveday, J. 2003, AJ, 125, 2276
Bonoli, S., Shankar, F., White, S., Springel, V., & Wyithe, S. 2010, MNRAS, in press (arXiv:0909.0003)
Boroson, T. 2005, AJ, 130, 381
Budavári, T., et al. 2001, AJ, 122, 1163
Carlberg, R. G. 1990, ApJ, 350, 505
Castander, F. J., et al. 2001, AJ, 121, 2331
Cavaliere, A., & Vittorini, V. 2000, ApJ, 543, 599
Coil, A. L., Hennawi, J. F., Newman, J. A., Cooper, M. C., & Davis, M. 2007, ApJ, 654, 115
Cole, S., & Kaiser, N. 1989, MNRAS, 237, 1127
Croft, R. A. C. 2004, ApJ, 610, 642
Croom, S. M., et al. 2005, MNRAS, 356, 415
da Ângela, J., et al. 2008, MNRAS, 383, 565
Djorgovski, S. 1991, in ASP Conf. Ser. 21, The Space Distribution of Quasars, ed. D. Crampton (San Francisco, CA: ASP), 349
Djorgovski, S. G. 1999, in ASP Conf. Ser. 193, The Hy-Redshift Universe: Galaxy Formation and Evolution at High Redshift, ed. A. J. Bunker & W. J. M. van Breugel (San Francisco, CA: ASP), 397
Djorgovski, S. G., Courbin, F., Meylan, G., Sluse, D., Thompson, D., Mahabal, A., & Glikman, E. 2007, ApJ, 662, L1
Djorgovski, S. G., Odewahn, S. C., Gal, R. R., Brunner, R. J., & de Carvalho, R. R. 1999, in ASP Conf. Ser. 191, Photometric Redshifts and the Detection of High Redshift Galaxies, ed. R. Weymann, L. Storrie-Lombardi, M. Sawicki, & R. Brunner (San Francisco, CA: ASP), 179
Djorgovski, S. G., Stern, D., Mahabal, A. A., & Brunner, R. 2003, ApJ, 596, 67
Djorgovski, S. G., Volonteri, M., Springel, V., Bromm, V., & Meylan, G. 2008, arXiv:0803.2862
Dunkley, J., et al. 2009, ApJ, 701, 1804
Efstathiou, G., & Rees, M. J. 1988, MNRAS, 230, 5P
Ellison, S. L., Hennawi, J. F., Martin, C. L., & Sommer-Larsen, J. 2007, MNRAS, 378, 801
Fan, X. 1999, AJ, 117, 2528
Fan, X., et al. 1999, AJ, 118, 1
Fan, X., et al. 2001, AJ, 122, 2833
Ferrarese, L., & Merritt, D. 2000, ApJ, 539, L9
Finlator, K., et al. 2000, AJ, 120, 2615
Fukugita, M., Ichikawa, T., Gunn, J. E., Doi, M., Shimasaku, K., & Schneider, D. P. 1996, AJ, 111, 1748
Fukugita, M., Nakamura, O., Schneider, D. P., Doi, M., & Kashikawa, N. 2004, ApJ, 603, L65
Gaskell, C. M. 1982, ApJ, 263, 79
Gebhardt, K., et al. 2000, ApJ, 539, L13
Gregg, M. D., Becker, R. H., White, R. L., Richards, G. T., Chaffee, F. H., & Fan, X. 2002, ApJ, 573, L85
Gunn, J. E., et al. 1998, AJ, 116, 3040
Gunn, J. E., et al. 2006, AJ, 131, 2332
Haehnelt, M. G., & Rees, M. J. 1993, MNRAS, 263, 168
Haiman, Z., Ciotti, L., & Ostriker, J. P. 2004, ApJ, 606, 763
Haiman, Z., & Hui, L. 2001, ApJ, 547, 27
Haiman, Z., & Loeb, A. 1998, ApJ, 503, 505
Häring, N., & Rix, H.-W. 2004, ApJ, 604, L89
Helmi, A., et al. 2003, ApJ, 586, 195
Hennawi, J. F. 2004, PhD thesis, Princeton Univ.
Hennawi, J. F., Dalal, N., & Bode, P. 2007a, ApJ, 654, 93
Hennawi, J. F., Dalal, N., Bode, P., & Ostriker, J. P. 2007b, ApJ, 654, 714
Hennawi, J. F., & Prochaska, J. X. 2007, ApJ, 655, 735
Hennawi, J. F., et al. 2006a, ApJ, 651, 61
Hennawi, J. F., et al. 2006b, AJ, 131, 1
Hopkins, P. F., Hernquist, L., Cox, T. J., Di Matteo, T., Robertson, B., & Springel, V. 2006, ApJS, 163, 1
Hopkins, P. F., Hernquist, L., Cox, T. J., & Kereš, D. 2008, ApJS, 175, 356
Hopkins, P. F., Lidz, A., Hernquist, L., Coil, A. L., Myers, A. D., Cox, T. J., & Spergel, D. N. 2007a, ApJ, 662, 110
Hopkins, P. F., Richards, G. T., & Hernquist, L. 2007b, ApJ, 654, 731
Hopkins, P. F., et al. 2004, AJ, 128, 1112
Hui, L., Stebbins, A., & Burles, S. 1999, ApJ, 511, L5
Inada, N., et al. 2006, ApJ, 653, L97
Inada, N., et al. 2003, Nature, 426, 810
Inada, N., et al. 2008, AJ, 135, 496
Infante, L., Varela, J., Moles, M., Hertling, G., García, A., & Menanteau, F. 2003, ApJ, 588, 90
Ivezić, Ž., et al. 2004, Astron. Nachr., 325, 583
Ivezić, Z., Tyson, J. A., Allsman, R., Andrew, J., & Angel, R. (LSST Collaboration) 2008, arXiv:0805.2366
Jiang, L., et al. 2006, AJ, 131, 2788
Jurić, M., et al. 2008, ApJ, 673, 864
Kaiser, N., et al. 2002, Proc. SPIE, 4836, 154
Kashikawa, N., Kitayama, T., Doi, M., Misawa, T., Komiyama, Y., & Ota, K. 2007, ApJ, 663, 765
Kauffmann, G., & Haehnelt, M. 2000, MNRAS, 311, 576
Kim, S., et al. 2009, ApJ, 695, 809
Kirkman, D., & Tytler, D. 2008, MNRAS, 391, 1457
Kochanek, C. S., Falco, E. E., & Muñoz, J. A. 1999, ApJ, 510, 590
Kundic, T. 1997, ApJ, 482, 631
Li, G. L., Mao, S., Jing, Y. P., Lin, W. P., & Oguri, M. 2007, MNRAS, 378, 469
Li, G. L., Mao, S., Jing, Y. P., Mo, H. J., Gao, L., & Lin, W. P. 2006, MNRAS, 372, L73
Lidz, A., Hopkins, P. F., Cox, T. J., Hernquist, L., & Robertson, B. 2006, ApJ, 641, 41
Lupton, R., Gunn, J. E., Ivezić, Z., Knapp, G. R., & Kent, S. 2001, in ASP Conf. Ser. 238, Astronomical Data Analysis Software and Systems X, ed. F. R. Harnden, Jr., F. A. Primini, & H. E. Payne (San Francisco, CA: ASP), 269
Lupton, R. H., Gunn, J. E., & Szalay, A. S. 1999, AJ, 118, 1406
Magorrian, J., et al. 1998, AJ, 115, 2285
Marconi, A., Risaliti, G., Gilli, R., Hunt, L. K., Maiolino, R., & Salvati, M. 2004, MNRAS, 351, 169
Martini, P., & Weinberg, D. H. 2001, ApJ, 547, 12
McDonald, P. 2003, ApJ, 585, 34
McDonald, P., & Miralda Escudé, J. 1999, ApJ, 518, 24
Miley, G. K., et al. 2004, Nature, 427, 47
Mo, H. J., & White, S. D. M. 1996, MNRAS, 282, 347
Mortlock, D. J., Webster, R. L., & Francis, P. J. 1999, MNRAS, 309, 836
Myers, A. D., Brunner, R. J., Nichol, R. C., Richards, G. T., Schneider, D. P., & Bahcall, N. A. 2007a, ApJ, 658, 85
Myers, A. D., Brunner, R. J., Richards, G. T., Nichol, R. C., Schneider, D. P., & Bahcall, N. A. 2007b, ApJ, 658, 99
Myers, A. D., Richards, G. T., Brunner, R. J., Schneider, D. P., Strand, N. E., Hall, P. B., Blomquist, J. A., & York, D. G. 2008, ApJ, 678, 635
Myers, A. D., et al. 2006, ApJ, 638, 622
Nusser, A., & Silk, J. 1993, ApJ, 411, L1
Oguri, M., et al. 2004, ApJ, 605, 78
Oguri, M., et al. 2005, ApJ, 622, 106
Oke, J. B., & Gunn, J. E. 1982, PASP, 94, 586
Oke, J. B., et al. 1995, PASP, 107, 375
Overzier, R. A., et al. 2006, ApJ, 637, 58
Overzier, R. A., et al. 2008, ApJ, 673, 143
Padmanabhan, N., White, M., Norberg, P., & Porciani, C. 2009, MNRAS, 397, 1862
Padmanabhan, N., et al. 2008, ApJ, 674, 1217
Pier, J. R., Munn, J. A., Hindsley, R. B., Hennessy, G. S., Kent, S. M., Lupton, R. H., & Ivezić, Ž. 2003, AJ, 125, 1559
Pooley, D., Blackburne, J. A., Rappaport, S., & Schechter, P. L. 2007, ApJ, 661, 19
Porciani, C., Magliocchetti, M., & Norberg, P. 2004, MNRAS, 355, 1010
Porciani, C., & Norberg, P. 2006, MNRAS, 371, 1824
Priddey, R. S., Ivison, R. J., & Isaak, K. G. 2008, MNRAS, 383, 289
Prochaska, J. X., & Hennawi, J. F. 2009, ApJ, 690, 1558
Richards, G. T., Vanden Berk, D. E., Reichard, T. A., Hall, P. B., Schneider, D. P., SubbaRao, M., Thakar, A. R., & York, D. G. 2002a, AJ, 124, 1
Richards, G. T., et al. 2001a, AJ, 121, 2308
Richards, G. T., et al. 2001b, AJ, 122, 1151
Richards, G. T., et al. 2002b, AJ, 123, 2945
Richards, G. T., et al. 2003, AJ, 126, 1131
Richards, G. T., et al. 2004, ApJS, 155, 257
Richards, G. T., et al. 2006, AJ, 131, 2766
Richards, G. T., et al. 2009, ApJS, 180, 67
Ross, N. P., et al. 2009, ApJ, 697, 1634
Schlegel, D. J., Finkbeiner, D. P., & Davis, M. 1998, ApJ, 500, 525
Schneider, D. P., et al. 2000, AJ, 120, 2183
Schneider, D. P., et al. 2005, AJ, 130, 367
Schneider, D. P., et al. 2007, AJ, 134, 102
Scranton, R., Connolly, A. J., Szalay, A. S., Lupton, R. H., Johnston, D., Budavari, T., Brinkman, J., & Fukugita, M. 2005, arXiv:astro-ph/0508564
Serber, W., Bahcall, N., Ménard, B., & Richards, G. 2006, ApJ, 643, 68
Sesar, B., et al. 2007, AJ, 134, 2236
Shankar, F. 2009, New Astronomy Reviews, 53, 57
Shankar, F., Bernardi, M., & Haiman, Z. 2009a, ApJ, 694, 867
Shankar, F., Cavaliere, A., Cirasuolo, M., & Maraschi, L. 2008, ApJ, 676, 131
Shankar, F., Crocce, M., Miralda Escudé, J., Fosalba, P., & Weinberg, D. H. 2010a, ApJ, 718, 321
Shankar, F., Salucci, P., Granato, G. L., De Zotti, G., & Danese, L. 2004, MNRAS, 354, 1020

Shankar, F., Sivakoff, G. R., Vestergaard, M., & Dai, X. 2010b, MNRAS, 401, 1869
Shankar, F., Weinberg, D. H., & Miralda-Escudé, J. 2009b, ApJ, 690, 20
Sheinis, A. I., Bolte, M., Epps, H. W., Kibrick, R. I., Miller, J. S., Radovan, M. V., Bigelow, B. C., & Sutin, B. M. 2002, PASP, 114, 851
Shen, Y. 2009, ApJ, 704, 89
Shen, Y., Strauss, M. A., Hall, P. B., Schneider, D. P., York, D. G., & Bahcall, N. A. 2008a, ApJ, 677, 858
Shen, Y., et al. 2007, AJ, 133, 2222
Shen, Y., et al. 2008b, ApJ, 680, 169
Shen, Y., et al. 2009, ApJ, 697, 1656
Shen, Y., et al. 2010, ApJ, 719, 1693 (Paper II)
Small, T. A., & Blandford, R. D. 1992, MNRAS, 259, 725
Smith, J. A., et al. 2002, AJ, 123, 2121
Smolčić, V., et al. 2004, ApJ, 615, L141
Soltan, A. 1982, MNRAS, 200, 115
Springel, V., et al. 2005, Nature, 435, 629
Steidel, C. C., Adelberger, K. L., Giavalisco, M., Dickinson, M., & Pettini, M. 1999, ApJ, 519, 1
Stephens, A. W., Schneider, D. P., Schmidt, M., Gunn, J. E., & Weinberg, D. H. 1997, AJ, 114, 41
Stiavelli, M., et al. 2005, ApJ, 622, L1
Stoughton, C., et al. 2002, AJ, 123, 485
Strand, N. E., Brunner, R. J., & Myers, A. D. 2008, ApJ, 688, 180
Thacker, R. J., Scannapieco, E., & Couchman, H. M. P. 2006, ApJ, 653, 86
Thacker, R. J., Scannapieco, E., Couchman, H. M. P., & Richardson, M. 2009, ApJ, 693, 552
Tremaine, S., et al. 2002, ApJ, 574, 740
Tucker, D. L., et al. 2006, Astron. Nachr., 327, 821
Turner, E. L. 1991, AJ, 101, 5
Tytler, D., & Fan, X.-M. 1992, ApJS, 79, 1
Vanden Berk, D. E., et al. 2001, AJ, 122, 549
Venemans, B. P., et al. 2002, ApJ, 569, L11
Venemans, B. P., et al. 2004, A&A, 424, L17
Venemans, B. P., et al. 2007, A&A, 461, 823
Walsh, D., Carswell, R. F., & Weymann, R. J. 1979, Nature, 279, 381
Weinstein, M. A., et al. 2004, ApJS, 155, 243
Wetzel, A. R., Cohn, J. D., & White, M. 2009a, MNRAS, 395, 1376
Wetzel, A. R., Cohn, J. D., & White, M. 2009b, MNRAS, 394, 2182
White, M., Martini, P., & Cohn, J. D. 2008, MNRAS, 390, 1179
Wolf, C., Wisotzki, L., Borch, A., Dye, S., Kleinheinrich, M., & Meisenheimer, K. 2003, A&A, 408, 499
Wyithe, J. S. B., & Loeb, A. 2002, ApJ, 581, 886
Wyithe, J. S. B., & Loeb, A. 2005, ApJ, 621, 95
Wyithe, S., & Loeb, A. 2008, arXiv:0810.3455
Yasuda, N., et al. 2001, AJ, 122, 1104
York, D. G., et al. 2000, AJ, 120, 1579
Yu, Q., & Tremaine, S. 2002, MNRAS, 335, 965
Zheng, W., et al. 2006, ApJ, 640, 574